Title

Identifying and treating CLN3 disease outside the central nervous system

Ewa A. Ziółkowska[1], Albina Jablonka-Shariff[2], Letitia L. Williams[1], Matthew J. Jansen[1], Sophie H Wang[1], Elizabeth M. Eultgen[1], Matthew D. Wood[2], Daniel A. Hunter[2], Jaiprakash Sharma[1], Marco Sardiello[1], Rebecca P. Bradley[5], Ineka T. Whiteman[6,7], Robyn Reese[8], Alan Pestronk[8], Mark S. Sands[3,4], Robert O. Heuckeroth[5], Alison K. Snyder-Warwick[2], Jonathan D. Cooper[1,4,8]

[1]Department of Pediatrics, Washington University in St. Louis, School of Medicine, St. Louis, MO 63110, USA
[2]Department of Surgery, Washington University in St. Louis, School of Medicine, St. Louis, MO 63110, USA
[3]Department of Medicine, Washington University in St. Louis, School of Medicine, St. Louis, MO 63110, USA
[4]Department of Genetics, Washington University in St. Louis, School of Medicine, St. Louis, MO 63110, USA
[5]Children's Hospital of Philadelphia Research Institute and Perelman School of Medicine at the University of Pennsylvania, Philadelphia, PA 19104, USA.
[6]Batten Disease Support, Research and Advocacy Foundation (US), P.O. Box 30049 Gahanna, OH 43230, USA.
[7]Batten Disease Support and Research Association (Australia), 74 McLachlan Avenue, Shelly Beach NSW 2261 Australia.
[8]Department of Neurology, Washington University in St. Louis, School of Medicine, St. Louis, MO 63110, USA

***Corresponding author**: Jonathan D. Cooper, Departments of Pediatrics, Genetics and Neurology, Washington University in St. Louis, School of Medicine, 660 S Euclid Ave, St Louis, MO 63110, USA. Phone: +1 (314) 273-9067. Fax +1 (314) 286-2894. E-mail: cooperjd@wustl.edu

Graphical abstract

Abstract

CLN3 disease causes profound neurological deficits in affected children, but less well recognized are a variety of peripheral neuromuscular and gastrointestinal problems. We hypothesized that in addition to central nervous system (CNS) degeneration, CLN3 deficiency may also directly affect neuronal and/or glial cell populations in the rest of the body. Therefore, we examined the neuromuscular and enteric nervous system in *Cln3*$^{\Delta ex7/8}$ mice. There was no overt sciatic nerve axon loss or demyelination in *Cln3*$^{\Delta ex7/8}$ mice, but significant loss of terminal Schwann cells (tSCs) at lower limb neuromuscular junctions (NMJ), and progressive NMJ denervation. This was accompanied by pronounced myofiber atrophy, with fewer and displaced myofibril nuclei, with similar pathology seen in a human CLN3 muscle biopsy. Atrophy was also evident in bowel smooth muscle with *Cln3*$^{\Delta ex7/8}$ mice displaying slow bowel transit, and significant loss of both enteric neurons and glial cells throughout the bowel. Similar enteric pathology was evident at autopsy in the small intestine and colon of a human CLN3 case. Neonatal administration of intravenous gene therapy to *Cln3*$^{\Delta ex7/8}$ mice using an AAV9-hCLN3 vector completely prevented tSCs and NMJ pathology, atrophy of both skeletal and smooth muscle, positively impacted bowel transit and largely prevented the loss of enteric neurons and glia. These findings reveal an underappreciated, but profound, impact of CLN3 disease outside the CNS and suggest these novel aspects of disease may be treatable using gene therapy.

Keywords

CLN3 disease, Batten disease, enteric nervous system, peripheral nervous system, neuromuscular junction, terminal Schwann cells, myopathy, AAV9, gene therapy

Introduction

Juvenile neuronal ceroid lipofuscinosis (JNCL; CLN3 disease) is a recessively inherited neurodegenerative disease, one of a larger group of disorders collectively called the neuronal ceroid lipofuscinoses (NCLs; Batten disease) [1-6]. CLN3 disease is caused by a mutation in the *CLN3* gene encoding a transmembrane protein [7], whose normal function remains elusive [8]. Nevertheless, CLN3-deficiency causes damage to the central nervous system (CNS), impairing the function of both neurons and glia, leading to profound neurodegeneration [9-17]. Indeed, it has been suggested that glial cells may play an active role in CLN3 pathogenesis, directly contributing to neuron loss [18-21]. The neurological effects of CLN3 disease have been thought to impact predominantly the CNS, resulting in blindness, epileptic seizures and mental disability [1,2,6,17]. However, it is apparent that CLN3 disease also causes a range of symptoms outside the CNS [1,2,6,17]. Such effects may occur secondary to degeneration within the CLN3 CNS, but we hypothesized that components of the nervous system, including both neurons and glia outside the CNS might also be negatively affected by CLN3 deficiency.

An important but often overlooked feature of CLN3 disease is severe gastrointestinal symptoms [6]. These symptoms include constipation, abdominal pain and bloating, and food intolerance, all of which negatively impact the quality of life and may impair the ability to absorb nutrients and drugs from the bowel, which in turn may lead to malnutrition. The enteric nervous system (ENS) controls many aspects of bowel function [22-26], including motility, and ENS defects can cause life-threatening disease [27-31]. The ENS is a complex network of at least 20 subtypes of enteric neurons, that interact with many different types of enteric glia, bowel smooth muscle and other cells to affect the relaxation and contraction of the bowel [22-27].

We have recently reported a severe impact upon the bowel in mouse models of CLN1 and CLN2 disease [32], with progressive loss of enteric neurons resulting in bowel dysmotility. To determine if the ENS is also compromised in CLN3 disease, we assessed bowel transit times and the

anatomical integrity of enteric neurons and glia in *Cln3*$^{\Delta ex7/8}$ mice at different stages of disease progression. These analyses revealed a progressive bowel transit defect that worsened with age, accompanied by loss of both enteric neurons and glia as well as smooth muscle atrophy in all bowel regions of *Cln3*$^{\Delta ex7/8}$ mice. Similar ENS pathology was present in a human CLN3 case.

Altered sensory and pain thresholds have been reported in children affected by multiple forms of NCL [1-6,33-35], in addition to impaired mobility and gait [6,17,36]. Each of these may be influenced by CNS degeneration, but very little is known about effects of CLN3 disease upon the peripheral nervous system (PNS) or neuromuscular system. Given the impact of CLN3 deficiency upon CNS astrocytes and microglia [12,13,18-21,37] we hypothesized that glia in the PNS may also be affected. In the PNS, the main type of glia are Schwann cells (SCs), which myelinate peripheral nerves [38-41]. However, there are also non-myelinating terminal Schwann cells (tSCs) that play important roles at both motor and sensory nerve endings [41-43]. These tSCs at the neuromuscular junction (NMJ) regulate NMJ functional stability and the integrity of skeletal muscle innervation [41-43]. Our analyses revealed very little impact of CLN3 deficiency upon either axon number or myelination of the sciatic nerve, but *Cln3*$^{\Delta ex7/8}$ mice had progressive loss of tSCs, progressive NMJ denervation, and pronounced atrophy of lower limb muscles, with evidence of myopathy. A human CLN3 muscle biopsy sample showed similar myopathic changes.

As a monogenic disorder, CLN3 disease is theoretically amenable to gene therapy [1-3,44]. CNS targeted gene therapy [45-47] would not be expected to completely treat either ENS or PNS manifestations of CLN3 deficiency. Therefore, we tested whether intravenous delivery of an adeno-associated viral vector (AAV9) expressing human CLN3 to neonatal *Cln3*$^{\Delta ex7/8}$ mice would prevent CLN3 disease effects in the bowel and neuromuscular system. AAV9-mediated gene therapy improved bowel transit and largely prevented the loss of enteric neurons and glia. This treatment also prevented the CLN3-disease associated loss of tSCs, NMJ denervation and myopathy in treated *Cln3*$^{\Delta ex7/8}$ mice. Taken together our data reveal novel and unexpected effects

of CLN3 deficiency outside the CNS and suggest these disease manifestations may be preventable by gene therapy.

Results

Bowel transit defects in Cln3$^{\Delta ex7/8}$ mice

To begin exploring the impact of CLN3 deficiency on gastrointestinal function we examined the bowel of *Cln3*$^{\Delta ex7/8}$ mice at disease endstage (18 months of age). At this age, *Cln3*$^{\Delta ex7/8}$ bowel appeared markedly distended, with stool filled proximal colon, cecum and distal small bowel **(Fig. 1A)**. This phenotype suggested bowel dysmotility in *Cln3*$^{\Delta ex7/8}$ mice, which we investigated by assessing bowel transit rates [32,48-50]. This phenotype is suggestive of bowel dysmotility in *Cln3*$^{\Delta ex7/8}$ mice, which we investigated by assessing bowel transit rates using Carmine red or FITC-labelled dextrans [32,48-50]. Whole bowel transit as assessed by Carmine red revealed a slower transit rate in *Cln3*$^{\Delta ex7/8}$ mice at disease mid-stage (12 months) compared to age-matched WT controls, although this difference was not statistically significant **(Fig. 1B)**. This transit of Carmine red worsened with age in both *Cln3*$^{\Delta ex7/8}$ and WT mice at disease end stage (18 months). Another measure of bowel transit is to analyze how far along the bowel FITC-labelled dextrans reach within 2 hours post gavage [32,48-50]. These analyses revealed that FITC-dextran had a similar distribution along the bowel in WT and *Cln3*$^{\Delta ex7/8}$ except for a tendency for more FITC-dextran in the distal small bowel (35% increase) and less in the cecum (43% decrease) and proximal colon (56% decrease) **(Fig. 1C)**, with weighted geometric means that were not statistically different between groups (data not shown). To examine the impact of CLN3 deficiency on distal colon motility, we evaluated colonic bead expulsion times [31,48-50]. While mean bead expulsion time was 7.78% longer in *Cln3*$^{\Delta ex7/8}$ mice compared to WT, this difference was not statistically significant **(Fig. 1D)**. Taken together, these data suggest *Cln3*$^{\Delta ex7/8}$ mice may have defective bowel motility that worsens with age, with striking distal small bowel, cecum and proximal colon distension, but

more subtle effects on bowel transit. Aging also prolongs bowel transit times in WT mice, but is less severe than that seen in *Cln3*$^{\Delta ex7/8}$ mice.

Progressive loss of enteric neurons in *Cln3*$^{\Delta ex7/8}$ mice

We hypothesized that bowel distension in *Cln3*$^{\Delta ex7/8}$ mice may be due to CLN3 disease effects upon the anatomic integrity of the ENS, which is compromised in other forms of NCL. To evaluate ENS myenteric neuron and glial cell density in small bowel and colon, we next stained bowel wholemount preparations from *Cln3*$^{\Delta ex7/8}$ mice and age-matched WT controls for the general neuronal marker HuC/D [31] and the intestinal glial marker S100B [31,51] revealing a similar organization of these markers in mice of both genotypes. Quantitative analysis confirmed no difference in the density of HuC/D positive neurons between WT and *Cln3*$^{\Delta ex7/8}$ mice in any bowel region at 1 month of age **(Supplementary Fig. S1)**, suggesting normal ENS development.

To investigate whether apparently normal ENS development in *Cln3*$^{\Delta ex7/8}$ mice was followed by progressive degeneration of enteric neurons, we next analyzed myenteric neuron density at disease mid stage (12 months) and end stage (18 months) after HuC/D immunostaining. Quantitative analyses showed significant reductions in the density of myenteric neurons in all bowel regions of *Cln3*$^{\Delta ex7/8}$ mice compared to WT controls **(Fig. 1E, 1F)** that became more pronounced with age. For example, myenteric neuron density in *Cln3*$^{\Delta ex7/8}$ duodenum, ileum, and colon was 21%, 22% and 35% lower than WT, respectively at 12 months of age. By disease end stage (18 months), *Cln3*$^{\Delta ex7/8}$ mice had only 42%, 41% and 48% of WT myenteric neuron density in duodenum, ileum and colon, suggesting progressive myenteric neuron loss **(Fig. 1F, Table 1)**. Enteric neuron loss was not evenly distributed in *Cln3*$^{\Delta ex7/8}$ myenteric plexus but occurred in patches with marked neuron loss adjacent to areas where neurons survived, and other areas where HuC/D-positive neurons appeared shrunken. These changes in enteric neuron density in

both small bowel and colon were accompanied by a corresponding decrease in staining for the neuron-specific microtubule marker TuJ1 in the *Cln3*$^{\Delta ex7/8}$ mice, that also became more pronounced with age **(Supplementary Fig. S2B)**. These data clearly indicate that there is a significant impact of CLN3 disease upon the integrity of enteric neurons in *Cln3*$^{\Delta ex7/8}$ mice.

Effects of CLN3 deficiency upon enteric glia and bowel macrophages

The normal function of the ENS also depends crucially upon populations of enteric glia and bowel macrophages [22-26], which may influence enteric neuron survival [52,53]. To investigate the impact of CLN3 disease upon enteric glia we stained bowel wholemounts from *Cln3*$^{\Delta ex7/8}$ mice for S100b and GFAP, two markers that are expressed by partially overlapping populations of enteric glia [51]. These analyses revealed an uneven and patchy distribution of GFAP immunoreactivity in the bowel of *Cln3*$^{\Delta ex7/8}$ mice **(Supplementary Fig. S2B),** with areas of both increased GFAP immunoreactivity in any bowel region, and other areas where GFAP immunoreactivity was markedly decreased. Areas with decreased GFAP immunoreactivity appeared to correlate with regions where decreased HuC/D neuron density was most pronounced. To determine whether *Cln3*$^{\Delta ex7/8}$ mice have fewer enteric glia than WT, we measured the density of S100B positive enteric glia at different levels of the bowel. Thhis analysis revealed significant reductions in the density of S100B positive enteric glia that only became apparent at disease endstage, with a 22% reduction in S100B glial density in duodenum and ileum of 18-month-old *Cln3*$^{\Delta ex7/8}$ mice, and 37% reduction in their colon **(Fig. 1G, Table 1).**

Human CLN3 disease small bowel displays ENS pathology

To examine the ENS in human CLN3 bowel, we obtained small bowel (ileum) and colon at autopsy from a 21-year-old girl with genetically confirmed CLN3 disease. Full thickness ileum

was pinned flat, fixed, stained with antibodies, cleared and then imaged as a wholemount preparation (without sectioning) using confocal microscopy to generate 3-dimensional images of the ENS [31,54-56] (**Fig. 2**). To compare to this CLN3 disease bowel, we similarly processed human ileum from a 17-year-old male undergoing surgery and colon from an 18-year-old female organ donor. Human bowel wholemount preparations were stained with antibodies to HuC/D (all nerve cell bodies), Tuj1 (to identify neurites), and SOX10 (to identify enteric glia). In these same regions we imaged autofluorescent storage material (AFSM), a hallmark of NCL neurodegenerative diseases [1-6]. These analyses revealed marked differences in the density of enteric neurons within ganglia (**Fig. 2A**) and regions where ganglia appeared to be missing, similar to findings in *Cln3*$^{\Delta ex7/8}$ mice. These changes were highly variable between ganglia, again resembling pathology in *Cln3*$^{\Delta ex7/8}$ mice. We also detected a pronounced accumulation of AFSM in HuC/D+ enteric neurons from the CLN3 disease ileum (**Fig. 2B**). At higher magnification, changes in the morphology of HuC/D positive neurons were evident in the CLN3 disease ileum (**Fig. 2B**), with fewer large neurons compared to the control organ donor small bowel (**Fig. 2B**). There were also markedly fewer SOX10+ glia in the human CLN3 disease ileum than in control ileum, with many SOX10+ HuC/D+ double positive cells in this human CLN3 disease ileum that were uncommon in control bowel (**Fig. 2B**). Similar effects were evident for colon enteric neurons in this CLN3 bowel, with fewer large neurons and a dramatic loss of Tuj1-positive neurites compared with the control organ donor colon (**Fig. 2C**). These data suggest CLN3 disease damages enteric neurons and glia in humans, similar to findings in *Cln3*$^{\Delta ex7/8}$ mice.

Lack of sciatic nerve axon loss and demyelination

We next explored whether neuronal and glial components of other PNS regions were affected by CLN3 deficiency. As a first step we examined the sciatic nerve, which contains both sensory and

motor peripheral axons and myelinating Schwann cells, using quantitative histomorphometry [57,58] to assess axon loss and demyelination in 18-month-old *Cln3*$^{\Delta ex7/8}$ mice **(Fig. 3A)**. This analysis revealed no statistically significant difference between axon number or axon area in these *Cln3*$^{\Delta ex7/8}$ mice **(Fig. 3A)**, compared to age-matched WT mice. There was also no evidence for sciatic nerve demyelination in *Cln3*$^{\Delta ex7/8}$ mice at this age **(Fig. 3A)**, with similar thickness of myelin in mice of both genotypes. The lack of significant morphological differences in the sciatic nerve, at an age when CNS pathology is already ongoing prompted us to further analyze neuromuscular components involved in the transmission of information to skeletal muscle.

Progressive loss of terminal Schwann cells and NMJ innervation.

Motor peripheral nerves end at the neuromuscular junction (NMJ), where incoming nerve fibers innervate the motor end-plate. The initial formation and subsequent stability of the NMJ is influenced by populations tSCs [41-43]. To obtain information about whether these different components of the NMJ are affected in *Cln3*$^{\Delta ex7/8}$ mice, we analyzed NMJ innervation, morphology, and tSC number and how these may change with disease progression **(Fig. 3B)**. We focused our analysis upon the extensor digitorum longus (EDL) as representative lower limb muscle. Detailed analysis of the NMJs revealed reduced tSC numbers in both WT and *Cln3*$^{\Delta ex7/8}$ mice between 12 and 18 months of age, but declines were far more pronounced in *Cln3*$^{\Delta ex7/8}$ mice than in age-matched controls **(Fig. 3C)**. In both genotypes there was also an increase in tSC fragmentation and an increased proportion of NMJs with atypical acetylcholine receptors (AChRs) as revealed by α-bungarotoxin (αBTX) between 12 and 18 months of age, both of which were more pronounced in *Cln3*$^{\Delta ex7/8}$ mice that in WT age-matched controls **(Fig. 3C)**. We next examined the innervation of NMJs by staining for neurofilament 200 (NF200) and found progressive increases in NMJ denervation in the EDL of mice of both genotypes, although this phenotype was much more pronounced in *Cln3*$^{\Delta ex7/8}$ mice **(Fig. 3D)**. In WT mice the percentage of partially innervated

(37.90%), and completely denervated NMJs (12.87%) was significantly higher in the EDL of 18-month-old with fewer completely innervated NMJs (84.49%), than was apparent at 12-month-old mice. However, in *Cln3*$^{\Delta ex7/8}$ mice there were already significant changes in the innervation of the NMJ at 12 months of age, compared to age-matched WT mice. This proportion of partially innervated (15%), and completely denervated NMJs (5.2%) at 12 months increased further in 18-month-old *Cln3*$^{\Delta ex7/8}$ mice. These data suggest an age-associated denervation of the EDL NMJ, which is exacerbated by CLN3 deficiency. Taken together these data suggest that CLN3 deficiency negatively impacts the NMJ, resulting in fewer tSCs and progressive denervation and that these effects are more pronounced than aging alone.

Evidence for myopathy in *Cln3*$^{\Delta ex7/8}$ mice and human CLN3 disease

To investigate whether NMJ pathology is accompanied by pathological changes in skeletal muscle in severely affected *Cln3*$^{\Delta ex7/8}$ mice, we performed routine H&E histology upon the quadriceps **(Fig. 4A)**, as a representative lower limb muscle. In 18-month-old *Cln3*$^{\Delta ex7/8}$ mice this analysis revealed a significant reduction in myofibril diameter, displacement of nuclei into the myofibril, reduction in the number of nuclei per myofibril **(Fig. 4B)**, and a pronounced extracellular deposition of ß-laminin between myofibrils **(Fig. 4A)**. To determine if similar muscle atrophy extended to smooth muscle, we also examined the bowel of *Cln3*$^{\Delta ex7/8}$ at the same age (**Fig 4C**). The thickness of the circular and longitudinal smooth muscle, and a combined measure of tunica muscularis were significantly thinner in all bowel regions of 18-month-old *Cln3*$^{\Delta ex7/8}$ vs. WT mice **(Fig. 4C**). Histological examination of the quadriceps muscle of a human CLN3 biopsy sample collected at 8 years of age revealed evidence of similar myofiber atrophy **(Fig. 4D)**, with multiple acid phosphatase positive granules in most muscle fibers, and in some muscle capillary endothelial cells. This human CLN3 biopsy specimen also displayed large punctate accumulations/aggregates immunoreactive for subunit c of mitochondrial ATP synthetase (SCMAS), a characteristic protein component of the

storage material that accumulates in the NCLs **(Fig. 4D)**, which were not present in a control biopsy. These data provide evidence for skeletal myopathy in *Cln3*$^{\Delta ex7/8}$ mice and suggest that similar muscle pathology is evident in human CLN3 disease relatively early in disease progression.

AAV9-mediated gene therapy preserves ENS structure and prevents bowel smooth muscle atrophy

Theoretically CLN3 deficiency is amenable to gene therapy [3,44], and CNS-directed gene therapy has positive treatment effects in *Cln3*$^{\Delta ex7/8}$ mice [45-47]. To apply a gene therapy strategy to CLN3 disease outside the CNS, we intravenously delivered 1.5 x 10^{11} vg/mouse of AAV9.hCLN3 to neonatal *Cln3*$^{\Delta ex7/8}$ mice and subsequently investigated the impact of this therapy upon the changes we had defined in ENS structure and function, and upon the neuromuscular system.

We first analyzed the effect of neonatal AAV9.hCLN3 treatment on bowel motility and ENS anatomical integrity. Compared to untreated *Cln3*$^{\Delta ex7/8}$ mice, our analyses showed an improvement in carmine red transit time in AAV9.hCLN3 treated *Cln3*$^{\Delta ex7/8}$ mice at both 12 and 18 months **(Fig. 5A)** but differences were not statistically significant. We next analyzed anatomic integrity of the ENS in wholemount bowel preparations from AAV9.hCLN3 treated *Cln3*$^{\Delta ex7/8}$ mice **(Fig. 5B)**. These analyses revealed a statistically significant protective effect of AAV9.hCLN3 treatment upon both HuC/D+ myenteric neurons and S100B+ myenteric glia **(Fig. 5B, 5C)**. In 18-month-old AAV9.hCLN3 treated *Cln3*$^{\Delta ex7/8}$ mice, the degree of HuC/D+ neuron loss was approximately half of than that seen in untreated *Cln3*$^{\Delta ex7/8}$ mice of the same age, with this effect evident along the entire length of the intestine and colon **(Fig. 5C, Table 1)**. For example, in the duodenum HuC/D+ neuron loss was to 42% of WT values in untreated *Cln3*$^{\Delta ex7/8}$ mice vs. 22% of WT values in AAV9.hCLN3 treated *Cln3*$^{\Delta ex7/8}$ mice; in the ileum HuC/D+ neuron loss was to 41% of WT values in untreated *Cln3*$^{\Delta ex7/8}$ mice vs. 20% of WT values in AAV9.hCLN3 treated *Cln3*$^{\Delta ex7/8}$ mice; in the colon HuC/D+

neuron loss was to 48% of WT values in untreated *Cln3*$^{\Delta ex7/8}$ mice vs. 27% of WT values in AAV9.hCLN3 treated *Cln3*$^{\Delta ex7/8}$ mice. There was lso a protective effect of AAV9.hCLN3 treatment upon the density of S100B+ enteric glia, which was significant in the distal part of the small intestine and in the colon. Finally, compared to untreated 18-month-old *Cln3*$^{\Delta ex7/8}$ mice, the thickness of the circular and longitudinal smooth muscle, and a combined measure of tunica muscularis were all significantly thicker in AAV9.hCLN3 treated *Cln3*$^{\Delta ex7/8}$ mice at the same age, appearing very similar to values from age-matched WT mice (**Fig. 6D**).

AAV9-mediated gene therapy prevents NMJ abnormalities and myopathy

We next analyzed the efficacy of neonatal AAV9.hCLN3 treatment up on lower limb NMJ and musculature. These analyses revealed a protective effect of AAV9.hCLN3 treatment upon both tSCs and NMJ innervation in 18-month-old *Cln3*$^{\Delta ex7/8}$ mice, upon lower limb myopathy and bowel smooth muscle atrophy (**Fig. 6**). The number of tSCs at the NMJ of AAV9.hCLN3 treated 18-month-old *Cln3*$^{\Delta ex7/8}$ mice was significantly greater than that seen in either untreated *Cln3*$^{\Delta ex7/8}$ mice or WT mice at this age and was comparable to that seen in 12-month-old WT mice **(Fig. 6A, 6B)**. Similarly, AAV9.hCLN3 treatment resulted in significantly more NMJs being completely innervated, and significantly fewer being either partially innervated or completely denervated **(Fig. 6C)**. Again, this treatment effect resulted in a pattern of NMJ innervation in 18-month-old AAV9.hCLN3 treated *Cln3*$^{\Delta ex7/8}$ mice that was indistinguishable from 12-month-old WT mice. AAV9.hCLN3 treatment also prevented the atrophy of bowel smooth muscle layers (**Fig 6D**), and of hind limb myofibers and deposition of ß-laminin between myofibrils, but did not completely prevent the decline in the number of nuclei per myofibril in *Cln3*$^{\Delta ex7/8}$ mice **(Fig. 6E)**.

Taken together, these data indicate that the neonatal administration of AAV9.hCLN3 gene therapy preserves NMJ structure and muscle innervation, and prevented skeletal myopathy and thinning of bowel smooth muscle.

Occurrence of liver tumors in AAV9.hCLN3 treated *Cln3*$^{\Delta ex7/8}$ mice

A well-recognized complication of intravenous gene therapy is the occurrence of hepatocellular carcinoma, especially at prolonged survival times [59,60]. To investigate whether this had occurred in our AAV9.hCLN3 treated *Cln3*$^{\Delta ex7/8}$ mice we examined liver. This revealed a localized dense mass of cells in the liver of 6 out of 10 treated *Cln3*$^{\Delta ex7/8}$ mice at 18 months. Histological analysis revealed morphology consistent with previously reported liver tumors following AAV treatments of this type. These data highlight the importance of titrating the vector dose, adjusting the time of administration and the need to find alternative vectors and/or capsids to transduce affected cells.

Discussion

To date CLN3 disease has been considered to predominantly affect the central nervous system [1,2,6,17]. However, effects of CLN3 deficiency outside the CNS are now emerging, with cardiac and autonomic phenotypes reported in affected children and young adults [61-65]. Our data reveal previously underrecognized effects of CLN3 disease that extend to both neuromuscular junction and enteric nervous system, along with myopathy of skeletal and bowel smooth muscle. These effects appear to involve both neuronal and glial pathology and may underlie or contribute to the debilitating neuromuscular and gastrointestinal problems of children with CLN3 disease [1,2,6,17], revealing new therapeutic targets that we show are treatable via gene therapy in mice. These data have important implications for targeting of therapies for CLN3 disease, highlighting additional need to treat extra-CNS pathology.

Given the neurological and neurodegenerative presentation of CLN3 disease [1,2,6,17], investigations into its pathogenesis and preclinical therapeutic strategies have primarily centered upon the CNS [1-6,45-47,66-74]. The progressive impact of CLN3 deficiency upon the brain is well recognized, and disease time course has been investigated in mouse models revealing prominent neurodegeneration that is preceded by localized activation of both astrocytes and microglia [12,13]. These CLN3 glia appear functionally compromised and may contribute to this neuron loss [18-21,37]. CNS directed AAV-mediated gene therapies have shown promising results in mice but only partial efficacy [44-46], which may be due to not effectively treating all affected regions of the CNS. Our data also suggest the presence of disease outside the CNS that is unlikely to be treated by brain-directed gene therapy.

In addition to direct effects upon the CNS, CLN3 disease affects many body systems, manifesting as cardiac arrhythmia, gastrointestinal symptoms, altered sensory thresholds, autonomic dysfunction, muscle rigidity or stiffness, clumsiness, and slow or dysregulated movements culminating in loss of ambulation [1,2,6,17,36,61-65]. These symptoms have largely been considered as manifestations of CNS neurodegeneration [6,17,66,67]. However, as our data emphasize, it is now becoming apparent that CLN3 disease directly affects cellular components outside the CNS. Proof of principle for this concept was first provided by reports of sinoatrial node pathology that may contribute to the cardiac dysfunction that many people with CLN3 disease display [6,17,61,62] that is treated by pacemaker implantation [75]. Our data from *Cln3*$^{\Delta ex7/8}$ mice provide further evidence for compromised neuron function both within the neuromuscular junction and within the bowel, and provide additional robust evidence that other cell types are pathologically impacted by CLN3 deficiency. This includes at least glia at the neuromuscular junction and within the enteric nervous system, skeletal muscle in the lower limb, and smooth muscle in the bowel. As such our data provide a novel perspective upon CLN3 disease pathogenesis and how the effects of CLN3 deficiency outside the CNS may be manifested at a cellular level

Muscular atrophy is a feature of the later stages of human CLN3 disease and other forms of NCL [1,2,6,17]. This may simply be a consequence of the inability of affected individuals to move [6,36]. This muscular atrophy may also be neurogenic in nature, due to reduced firing of the nerves innervating skeletal muscle as a consequence of neurodegeneration within the CNS [9-16]. However, the lack of significant axon loss within the sciatic nerve of disease-end stage *Cln3*$^{\Delta ex7/8}$ mice suggests other cellular mechanisms may operate. Our data provide the first evidence of a pathological impact of CLN3 disease upon the NMJ and provide clues about how this may arise. Terminal Schwann cells play important roles in regulating NMJ stability and maintaining nerve terminals [41-43]. The progressive loss of tSCs we documented in *Cln3*$^{\Delta ex7/8}$ mice, is a novel finding and may plausibly cause the NMJ denervation that accompanies it. Our data suggest this NMJ phenotype is also evident in normal aging but is exacerbated by CLN3 deficiency. Whether this reflects a direct consequence of CLN3 deficiency upon this functionally important glial cell type remains poorly understood, but our data about AChR morphology, and tSC loss or fragmentation suggest other pathological mechanisms may contribute to NMJ pathology.

Based on evidence from primary neuromuscular disorders [76,77], and from Pompe disease (another lysosomal storage disorder) [78], both tSC cell loss and NMJ denervation can occur secondary to primary myopathy or degenerative effects of skeletal muscle. Reports of muscle pathology in CLN3 disease are rare and largely limited to ultrastructural observations in human CLN3 cases [79-81], apart from some recent reports of vacuolar myopathy [82,83]. As such, our data for myofiber atrophy and other pathological effects within the quadriceps provide the first quantitative analyses of skeletal muscle abnormalities in CLN3 disease. The reduction in myofiber nuclear number, displacement of nuclei, and changes in the extracellular matrix are all evidence of muscle pathology in *Cln3*$^{\Delta ex7/8}$ mice at disease end stage. Similar findings are also evident in a human CLN3 muscle biopsy sample taken at 8 years of age, relatively early in disease progression, suggesting this muscle pathology is not a late onset consequence of CLN3 disease.

Before definitive conclusions can be drawn about whether pathology observed represents primary myopathy, further investigations are necessary. It will be important to detail the onset and progression of skeletal muscle pathology, whether this differs between muscles of different types and in different anatomical locations, and how this relates mechanistically to events at the NMJ and within the CNS. It will also be informative to determine if similar NMJ and myopathy phenotypes are present in other forms of NCL.

The atrophy of bowel smooth muscle that we documented in both small intestine and colon of *Cln3*$^{\Delta ex7/8}$ mice, suggests that the pathological effects of CLN3 deficiency impact both striated and smooth muscle. This novel phenotype could plausibly result in the bowel dilation we observed, but given the significant role played by the ENS upon many aspects of bowel function [22-27] it is likely that the profound loss of enteric neurons and glia in all bowel regions of *Cln3*$^{\Delta ex7/8}$ mice also contributes significantly to bowel dysfunction. These new data are consistent with our recent characterization of CLN1 and CLN2 mice that model earlier onset forms of NCL and also display significant progressive enteric neuron degeneration and bowel transit defects [32]. A distinguishing feature of ENS pathology in *Cln3*$^{\Delta ex7/8}$ mice is that enteric glia are affected to a greater extent than in either CLN1 or CLN2 mice [32], and may hint at different cellular mechanisms being involved, as is becoming evident in the CNS [17,66,67]. Studies are underway to address the underlying molecular mechanisms and the cellular specificity of these effects upon neurons and glia. Nevertheless, our data collectively point to ENS disease and bowel dysmotility being present in multiple forms of NCL. Importantly, ENS pathology also appears to occur in human NCL, with archival case reports briefly mentioning the presence of storage material in myenteric plexus neurons in multiple forms of NCL [79-81,84,85]. We have supplemented these observations by recently demonstrating that ENS pathology is also present in human CLN1 autopsy material [32], and this study confirms this phenotype also extends to CLN3 disease.

Clinical implications

Our data consistently show a pathological impact upon both neuronal and glial components in the bowel and neuromuscular system of *Cln3*$^{\Delta ex7/8}$ mice. These disease manifestations are unlikely to be treated by CNS-directed gene therapy, and incomplete treatment of CLN3 disease outside the CNS may explain the incomplete efficacy of CNS-directed therapies [44-46]. In this respect, our data demonstrating efficacy of neonatal intravenous administration of AAV-mediated gene therapy, provides proof of principle that these newly identified features of CLN3 disease might also be amenable to gene therapy. We have previously used this strategy to treat enteric disease in CLN1 and CLN2 disease mice, preventing bowel transit defects and extending the lifespan of these mice [32]. In these lysosomal enzyme deficient forms of NCL, where cross correction by secreted enzyme is possible (since lysosomal enzymes are taken up by adjacent cells and traffic to the lysosome), gene therapy vectors do not need to transduce every cell to have therapeutic effects. In this respect, our data revealing that AAV9.hCLN3 treatment had positive effects upon the bowel phenotypes of *Cln3*$^{\Delta ex7/8}$ mice is encouraging. There may be room for further improvement by using cell-type specific promoters to drive hCLN3 expression in affected cell types. However, the same CAG promoter AAV9.hCLN3 virus had remarkably positive effects upon the neuromuscular system, almost completely preventing all of the pathologies at the NMJ and most pathology evident in skeletal muscle. It remains to be seen whether these treatment effects are due to the higher extent to which AAV9 transduces skeletal muscle compared to tSCs. However, it is possible that the beneficial effects of our AAV9.hCLN3 gene therapy upon the NMJ are due to correcting the effects of disease upon skeletal muscle, via treating tSCs themselves or a combination of these events.

Similar therapeutic effects of gene therapy have been reported in the muscle and NMJ of Pompe disease mice [86], highlighting the potential broad applicability of AAV-mediated gene therapy to treat multiple lysosomal storage disorders. Our data further raise the possibility that an intravenous

gene therapy strategy could treat several extra-CNS consequences of CLN3 disease. Nevertheless, intravenous delivery for AAV9 does not appear very efficient at treating the NCL CNS [32], and combined treatments that target both extra- and intra-CNS pathology are likely to be needed. Another key consideration is the occurrence of hepatocellular carcinoma in a subset of our AAV9.hCLN3 treated *Cln3*$^{\Delta ex7/8}$ mice. This is a well-recognized complication of intravenous AAV9 gene therapy [59,60], and strategies will be needed to mitigate this risk. This may include delaying vector administration but there is a need to identify capsid variants and vectors that limit transduction of liver cells and instead target AAVs to the most affected cell types.

MATERIALS AND METHODS

Human bowel autopsy samples

Human CLN3 bowel samples were obtained with fully informed consent from an individual confirmed to be homozygous for the 1.02kb deletion in in the *CLN3 g*ene, and shared with investigators as a de-identified sample. This individual showed a typical CLN3 disease onset and died at 21 years of age. The use of this de-identified sample at Washington University in St. Louis was Institutional Review Board exempt. The control 18-year-old human colon was an organ donor, while the 17-year-old human ileum was from a de-identified subject who had surgery at Children's Hospital of Philadelphia (CHOP) with approval of CHOP's IRB (IRB 13-010357). Organ donor colon was from the Gift of Life Donor Program (also Institutional Review Board exempt).

Human muscle biopsy samples

The muscle biopsy samples were originally performed for clinical purposes. These samples were from an individual confirmed to to be homozygous for the 1.02kb deletion in the *CLN3 g*ene, who showed a typical CLN3 disease onset with the biopsy collected at 8 years of age (representing early stage CLN3 disease). The control sample was from an 11-year-old individual who had normal gene testing. These samples were retrospectively analyzed under Washington University in St. Louis, School of Medicine IRB approval numbers 201101855 & 201104149. No informed consent was required for this retrospective study of de-identified muscle specimens.

Mice

Cln3$^{\Delta ex7/8}$ mice [87], and wild type (WT) mice were maintained separately on a congenic C57Bl/6J background at Washington University School of Medicine. Mice were provided food and water *ad libitum* under a 12hr light/dark cycle. Numbers analyzed are detailed in Figures, but all studies used balanced numbers of males and females. These studies follow ARRIVE guidelines and were performed under protocols 2018-0215, 21-0292 and 24-0232 approved by the Institutional Animal

Care and Use Committee (IACUC) at Washington University School of Medicine in St. Louis, MO and The Children's Hospital of Philadelphia IACUC protocol IAC 22-001041.

Bowel transit studies

Whole bowel transit: Mice fasted overnight were gavage-fed with 6% carmine red dye (300 µl) Sigma-Aldrich) in distilled water containing 0.5% methylcellulose (Sigma-Aldrich) and placed in individual cages with white paper covering cage bottoms. Passage of red stool was evaluated at 10 min intervals. Each mouse was tested three times with ~3 days between tests, as previously described [32,46-48].

FITC-dextran transit: Mice fasted overnight were gavage-fed with 100 µL FITC-Dextran (10 mg/mL, 70,000 MW; MilliporeSigma) in distilled water containing 2% methylcellulose (MilliporeSigma). After 2 hours, bowel from isoflurane-euthanized mice was divided into 15 segments (small intestine 1–10, proximal and distal cecum, colon 1–3). Segment contents were suspended in 100 µL 1X phosphate buffered saline, vortexed 15 s, and centrifuged (4000 rpm, 10 min). Supernatant fluorescence was measured (excitation 485 nm, emission at 525 nm). Weighted geometric mean (sum of segment number × (FITC fluorescence in that segment)/total FITC fluorescence) was calculated as described [32,46-48].

Colonic bead expulsion: Mice were anesthetized with isoflurane (1.5 min). A glass bead (3 mm, MilliporeSigma) lubricated with sunflower seed oil (MilliporeSigma) was inserted 2 cm into the colon using a custom-made 3 mm diameter rounded glass rod. Anesthesia was stopped and bead expulsion time was recorded. Assay was repeated 3 times per mouse with >48 hours between procedures [32,48-50].

Human bowel wholemount immunostaining and imaging

Wholemount specimens of human bowel were processed via a previously published clearing and immunostaining protocol [54-56]. Briefly, following trimming of visceral fat and fixation, 5 mm x 5 mm full thickness pieces of bowel were washed in PBS, permeabilized with 100% methanol, treated with Dent's bleach and placed in blocking solution (3 days on a shaker at 37°C). This was followed by incubation in primary antibody (Supplementary Table 1) (14 days at 37°C) on a shaker. Tissue was then washed in PBS followed by incubation in secondary antibody (Supplementary Table 1) (3 days at 37°C) on a shaker, dehydrated in serial methanol dilutions, and cleared with benzyl alcohol-benzyl benzoate (BABB) (1:2) until tissue was translucent (~24 hours). Tissue was transferred to ethyl cinnamate and mounted on glass slides in ethyl cinnamate for imaging via confocal microscopy within 5 days of tissue clearing [54-56].

Cleared human bowel tissue was imaged on a Zeiss LSM 980 confocal microscope (10x/0.3 and 20x/0.8 Plan-Apochromat objectives, and *Zen* 3.5.093.00003 software (Zeiss, Oberkochen, Germany). *Z*-axis intervals were 4 mm (10x objective) or 1 mm (20x objective). For each segment imaged, confocal Z-stacks were obtained with 10x objective using tile scan (5% overlap) and stitch features to visualize large regions of full-thickness tissue. Multichannel images were acquired sequentially using laser-scanning operated under multitrack. Excitation/ long-pass emission filters were Alexa Fluor 594, and Alexa Fluor 647. Excitation/ long-pass emission filter Alexa Fluor 488 was used to capture ASFM autofluorescence [54-56].

Wholemount bowel histology in mice

Mice were anesthetized (2% isoflurane) and transcardially perfused with PBS and decapitated. The first and last 8 cm of small intestine and entire colon were cut into 2 cm lengths in cold 50 mM Tris buffered saline (TBS, pH=7.6), opened along mesenteric border, pinned to Sylgard™ 184 Silicone Elastomer (Dow Corning) using insect pins, and fixed in fresh 4% paraformaldehyde (35 minutes colon, 45 minutes ileum, 1 hour duodenum) [32]. Fixed tissue was stored in TBS/0.1%

sodium azide (4°C) before staining for neuronal or glial markers [32,46-48]. Muscle layers (1 cm lengths) separated from mucosa and submucosa were blocked (1 hour) in TBS containing 4% Triton X-100 (TBST), 15% normal goat serum (NGS) (Jackson Immuno-Research Laboratories), then incubated in primary antibody (Supplemental Table 1) at 4°C overnight, washed (3x, TBS), and incubated in secondary antibodies (Supplemental Table 1) in 10% goat serum, 4% TBST for 2 hours. Bowel was mounted on Colorfrost plus (Thermo Fisher Scientific) slides, dried briefly before incubation in 1x solution TrueBlack lipofuscin autofluoresence quencher (Biotium) in 70% ethanol (5 min) and rinsing (1xTBS). Slides were coverslipped in Fluoromount-G mounting medium containing DAPI (Southern Biotech) [32,48-50].

Quantitative analysis of immunostained mouse bowel

Unless otherwise specified, 10 systematically sampled regularly spaced 20× fields (each 0.42250 mm^2) per sample were analyzed [32,48-50]. Multi-channel images were collected on a Zeiss AxioImager Z1 microscope using StereoInvestigator (MBF Bioscience) software and exported to ImageJ (NIH). Myenteric neurons (HuC/D+ cells) and enteric glia (S100B+ cells) were manually counted in each field and averaged to determine cells/mm^2 [32,48-50]. All analyses were made blind to genotype or treatment.

Sciatic Nerve staining and Analyses

Harvested nerve samples (n = 6 per group) were fixed in 3% Electron Microscopy grade glutaraldehyde (Polysciences, Warrington, PA) at 4 °C, postfixed with 1% osmium tetroxide, and serially dehydrated in ethanol. Specimens were embedded in Araldite 502 (Polysciences), and cut into 1 μm cross-sections with an ultramicrotome (LKB III Produkter A.B., Bromma, Sweden). For imaging by light microscopy, sections were stained with 1% toluidine blue dye, a reproducible method of quantitative peripheral nerve assessment, and mounted on slides [57,58].

Quantitative analysis was performed with a semi-automated digital image analysis system linked to Clemex PE software adapted for nerve morphometry (Clemex Technologies Inc., Longueuil, Quebec) [58]. Clemex PE allows generation of analysis method using sequential selection of standard workflows and thus negates the need for programming. The workflow used is adapted from our previous work [58] and is available from us in Clemex PE upon request. Briefly, sectioned nerve images were divided into 100 × 100 μm^2 non-overlapping frames and evaluated using eight-bit plane digital pseudo-coloring and thresholding-based algorithms to identify myelinated axons, calculate their density, area, myelin thickness, and diameters [58].

Immunofluorescence and Quantitative NMJ analyses

Extensor digitorum longus (EDL) muscles from *Cln3*$^{\Delta ex7/8}$ and control WT mice were dissected and fixed overnight at 4C in 4% paraformaldehyde for histological analysis. EDL wholemounts and longitudinal frozen sections (25 μm thickness) of muscle were stained by immunofluorescence as previously described [88], with incubation in primary and secondary antibodies (Supplementary Table 1). Slides were prepared using Vecta shield mounting medium with DAPI to label nuclei. NMJs were imaged with an AxioImager M2 fluorescent microscope (CarlZeiss) and analyzed using NIH ImageJ [88]. For analyses over 100 NMJs per muscle were analyzed. Three NMJ components were examined: tSCs (S100B antibody), presynaptic nerve terminals (NF200 antibody), and postsynaptic motor end plates (αBTX) [82]. To determine the percentage of normal and atypical endplates, the number of fragments per end plate was counted. End plates were considered normal if AChRs formed a continuous, “pretzel-like” structure with ≤7 fragments and regular overall size [88]. An NMJ was defined as fully innervated if nerve and end plate clusters aligned over ≥75% of their length [88]. Denervation was defined as no overlap of neurofilaments and αBTX staining. The percentage of innervated NMJs was normalized to the total number of NMJs in the macroscopic field of view.

Muscle histology and Analyses

Immediately after decapitation, the quadriceps femoris and jejunum were harvested and fixed overnight at 4C in fresh 4% paraformaldehyde. The fixed tissues were embedded in paraffin blocks and sectioned at 10 µm thickness using a sledge microtome. Sections were deparaffinized and stained with haematoxylin and eosin, or acid phosphatase according to standard protocols. A minimum of 300 muscle fibres were measured in the quadriceps per individual. Additionally, the quadriceps femoris was stained for ß-laminin to assess the extracellular deposits between muscle fibres. The thickness of individual bowel smooth muscle layers was measured in at least 5 sections per individual, with 10 measurements made in each section.

Intravenous gene therapy

Injections employed a AAV9 virus expressing human CLN3 (hCLN3). This is essentially the same virus used in our CNS studies in CLN1 disease mice [89-95] and described previously in detail [89], but expressing the hCLN3 sequence instead of the PPT1 sequence. Virus was packaged at University of North Carolina Vector Core. Virus injections 1.5×10^{11} vg/mouse were made into the superficial temporal vein of hypothermia-anesthetized neonatal (P1) mice [32]. Neonatally injected mice were returned to their mothers, raised until weaning, and were aged until predicted disease endstage, at which point most analyses were conducted.

Statistical analyses

Statistical analyses were performed using GraphPad Prism version 9.1.0 for MacOS (GraphPad Software, San Diego, CA). A one-way ANOVA with a post-hoc Bonferroni correction was used for comparison between three groups or more. A p-value of ≤ 0.05 was considered significant.

Study Approval: All animal procedures were performed in accordance with National Institutes of Health (NIH) guidelines under protocols 2018-0215 and 21-0292 approved by the Institutional Animal Care and Use Committee (IACUC) at Washington University School of Medicine in St.

Louis, MO; and The Children's Hospital of Philadelphia IACUC protocol IAC 22-001041. The analysis of de-identified human autopsy material was reviewed by the Institutional Review Board of Washington University School of Medicine in St. Louis, MO and was considered not to meet the definition of human research, and therefore exempt from IRB approval. The human muscle biopsy samples were originally performed for clinical purposes. These samples were retrospectively analyzed under Washington University in St. Louis, School of Medicine IRB approval numbers 201101855 & 201104149. No informed consent was required for this retrospective study. Organ donor colon was from the Gift of Life Donor Program (also Institutional Review Board exempt).

Data Availability Statement: All the data from this study will be made available to other researchers.

Authors' contributions: JDC, ROH, MSS, AKW conceived and designed the study and obtained funding; EAZ, MJJ, JDC, and SHW carried out the bowel preparation; EAZ performed mouse bowel and skeletal muscle immunostaining and quantitative analyses; EAZ prepared all the figures with JDC; LLW performed bowel transit studies, with initial input from KT; EME managed the mouse colonies, generated the mice for these studies and performed all genotyping; EAZ performed muscles histology, staining and analyses; ASW and AJS performed the NMJ analyses; MDW and DAH performed the quantitative analyses of sciatic nerve histology; MS and JPS constructed the AAV9-CLN3 vector used in these studies; ITW made the arrangements for donation and collection of the human CLN3 bowel, liaising with the family and health care facility to arrange informed consent; RPB performed the human bowel wholemount immunostaining and imaged this under the supervision of ROH; RR and AP performed the histological analyses of human muscle samples; MSS and LLW performed the neonatal vector administration; JDC, ASW, MSS and ROH supervised all studies; JDC, ASW, MSS, ROH and EAZ interpreted data; JDC and EAZ wrote the manuscript with input from all the authors. All authors read and approved the final manuscript.

Acknowledgments: This study was initiated directly from discussions with affected Batten disease families about their gastrointestinal and neuromuscular symptoms, and we thank them for sharing their experiences and inspiring this work. We would particularly like to thank the families of the children with CLN3 disease for their generosity in donating the samples for our research, and all involved in the collection and preservation of these samples. The ANNA-1 anti-HuC/D antibody was kind gift of Dr. Vanda A Lennon, Mayo Clinic, Rochester, MN. We thank Drs. Tom Gillingwater, Tom Wishart and Alison Barnwell for constructive comments on the manuscript.

Funding: This project was supported by grants to JDC from the Fore Batten Foundation, the Children's Brain Diseases Foundation institutional support from the Department of Pediatrics, Washington University in St. Louis to JDC; Irma and Norman Braman Endowment to ROH, Suzi and Scott Lustgarten Center Endowment to ROH, The Children's Hospital of Philadelphia Frontier Program Center for Precision Diagnosis and Therapy for Pediatric Motility Disorders to ROH, R01DK129691 to ROH, and NINDS National Institutes of Health grants R01 NS100779 to MSS; R21 NS116574, R21 NS126907 and R01 NS124655 to JDC.

Competing interests: JDC has received research support from BioMarin Pharmaceutical Inc., Abeona Therapeutics Inc., REGENXBIO Inc. and Neurogene, and is a consultant for JCR Pharmaceuticals. ROH was a consultant for BlueRock Therapeutics and served on a Scientific Advisory Board for Takeda. The remaining authors declare no conflicts of interest.

References

1. Kohlschütter A, Schulz A, Bartsch U, Storch S. Current and Emerging Treatment Strategies for Neuronal Ceroid Lipofuscinoses. *CNS Drugs*. 2019; 33(4):315-325.

2. Mole SE, Anderson G, Band HA, Berkovic SF, Cooper JD, Kleine Holthaus SM, McKay TR, Medina DL, Rahim AA, Schulz A, Smith AJ. Clinical challenges and future therapeutic approaches for neuronal ceroid lipofuscinosis. *Lancet Neurol*. 2019; 18:107-16.

3. Johnson TB, Cain JT, White KA, Ramirez-Montealegre D, Pearce DA, Weimer JM. Therapeutic landscape for Batten disease: current treatments and future prospects. *Nat Rev Neurol.* 2019; 15:161-78.

4. Augustine EF, Adams HR, de Los Reyes E, Drago K, Frazier M, Guelbert N, Laine M, Levin T, Mink JW, Nickel M, Peifer D, Schulz A, Simonati A, Topcu M, Turunen JA, Williams R, Wirrell EC, King S. Management of CLN1 Disease: International Clinical Consensus. *Pediatr Neurol.* 2021; 120:38-51.

5. Mole SE, Schulz A, Badoe E, Berkovic SF, de Los Reyes EC, Dulz S, Gissen P, Guelbert N, Lourenco CM, Mason HL, Mink JW, Murphy N, Nickel M, Olaya JE, Scarpa M, Scheffer IE, Simonati A, Specchio N, Von Löbbecke I, Wang RY, Williams RE. Guidelines on the diagnosis, clinical assessments, treatment and management for CLN2 disease patients. *Orphanet J Rare Dis*. 2021; 16(1):185.

6. Ostergaard JR. Juvenile neuronal ceroid lipofuscinosis (Batten disease): current insights. *Degener Neurol Neuromuscul Dis*. 2016; 6:73-83.

7. International Batten Disease Consortium. Isolation of a novel gene underlying Batten disease, CLN3. *Cell* 1995; 82:949-57

8. Laqtom NN, Dong W, Medoh UN, Cangelosi AL, Dharamdasani V, Chan SH, Kunchok T, Lewis CA, Heinze I, Tang R, Grimm C, Dang Do AN, Porter FD, Ori A, Sabatini DM, Abu-Remaileh M. CLN3 is required for the clearance of glycerophosphodiesters from lysosomes. *Nature* 2022; 609(7929):1005-1011.

9. Anderson GW, Goebel HH, Simonati A. Human pathology in NCL. *Biochim Biophys Acta*. 2013; 1832(11):1807-26.

10. Tyynelä J, Cooper JD, Khan MN, Shemilt SJ, Haltia M. Hippocampal pathology in the human neuronal ceroid-lipofuscinoses: distinct patterns of storage deposition, neurodegeneration and glial activation. *Brain Pathol.* 2004; 14(4):349-57.

11. Hachiya Y, Hayashi M, Kumada S, Uchiyama A, Tsuchiya K, Kurata K. Mechanisms of neurodegeneration in neuronal ceroid-lipofuscinoses. *Acta Neuropathol*. 2006; 111(2):168-77.

12. Pontikis CC, Cella CV, Parihar N, Lim MJ, Chakrabarti S, Mitchison HM, Mobley WC, Rezaie P, Pearce DA, Cooper JD. Late onset neurodegeneration in the Cln3-/- mouse model of juvenile neuronal ceroid lipofuscinosis is preceded by low level glial activation. *Brain Res*. 2004; 1023(2):231-42.

13. Pontikis CC, Cotman SL, MacDonald ME, Cooper JD. Thalamocortical neuron loss and localized astrocytosis in the Cln3Deltaex7/8 knock-in mouse model of Batten disease. *Neurobiol Dis.* 2005; 20(3):823-36.

14. Weimer JM, Benedict JW, Elshatory YM, Short DW, Ramirez-Montealegre D, Ryan DA, Alexander NA, Federoff HJ, Cooper JD, Pearce DA. Alterations in striatal dopamine catabolism precede loss of substantia nigra neurons in a mouse model of juvenile neuronal ceroid lipofuscinosis. *Brain Res*. 2007; 1162:98-112.

15. Weimer JM, Custer AW, Benedict JW, Alexander NA, Kingsley E, Federoff HJ, Cooper JD, Pearce DA. Visual deficits in a mouse model of Batten disease are the result of optic nerve degeneration and loss of dorsal lateral geniculate thalamic neurons. *Neurobiol Dis*. 2006; 22(2):284-93.

16. Weimer JM, Benedict JW, Getty AL, Pontikis CC, Lim MJ, Cooper JD, Pearce DA. Cerebellar defects in a mouse model of juvenile neuronal ceroid lipofuscinosis. *Brain Res*. 2009; 1266:93-107.

17. Ostergaard JR, Nelvagal HR, Cooper JD. Top-down and bottom-up propagation of disease in the neuronal ceroid lipofuscinoses. *Front Neurol*. 2022; 13:1061363.

18. Xiong J, Kielian T. Microglia in juvenile neuronal ceroid lipofuscinosis are primed toward a pro-inflammatory phenotype. *J Neurochem*. 2013; 127(2):245-58.

19. Burkovetskaya M, Karpuk N, Xiong J, Bosch M, Boska MD, Takeuchi H, Suzumura A, Kielian T. Evidence for aberrant astrocyte hemichannel activity in Juvenile Neuronal Ceroid Lipofuscinosis (JNCL). *PLoS One*. 2014; 9(4):e95023.

20. Parviainen L, Dihanich S, Anderson GW, Wong AM, Brooks HR, Abeti R, Rezaie P, Lalli G, Pope S, Heales SJ, Mitchison HM, Williams BP, Cooper JD. Glial cells are functionally impaired in juvenile neuronal ceroid lipofuscinosis and detrimental to neurons. *Acta Neuropathol Commun*. 2017; 5(1):74.

21. Takahashi K, Nelvagal HR, Lange J, Cooper JD. Glial Dysfunction and Its Contribution to the Pathogenesis of the Neuronal Ceroid Lipofuscinoses. *Front Neurol*. 2022; 13:886567.

22. Schneider S, Wright CM, Heuckeroth RO. Unexpected Roles for the Second Brain: Enteric Nervous System as Master Regulator of Bowel Function. *Annu Rev Physiol*. 2019; 81:235-259.

23. Sharkey KA, Mawe GM. The enteric nervous system. *Physiol Rev*. 2023; 103:1487-1564.

24. Gonzales J, Gulbransen BD. The Physiology of Enteric Glia. *Annu Rev Physiol*. 2024. doi: 10.1146/annurev-physiol-022724-105016. Online ahead of print.

25. Windster JD, Kakiailatu NJM, Kuil LE, Antanaviciute A, Sacchetti A, MacKenzie KC, Peulen-Zink J, Kan TW, Bindels E, de Pater E, Doukas M, van den Bosch TPP, Yousefi S, Barakat TS, Meeussen CJHM, Sloots PCEJ, Wijnen RMH, Parikh K, Boesmans W, Melotte V, Hofstra RMW, Simmons A, Alves MM. *Gastroenterology*. 2024 Dec 24:S0016-5085(24)05803-7.

26. Lou M, Heuckeroth RO, Tjaden NEB. Neuroimmune Crossroads: The Interplay of the Enteric Nervous System and Intestinal Macrophages in Gut Homeostasis and Disease. *Biomolecules*. 2024; 14(9):1103.

27. Lake JI, Heuckeroth RO. Enteric nervous system development: migration, differentiation, and disease. *Am J Physiol Gastrointest Liver Physiol*. 2013; 305(1):G1-24.

28. Furness JB. The enteric nervous system: normal functions and enteric neuropathies. *Neurogastroenterol Motil*. 2008; 20 Suppl 1:32-8.

29. Di Nardo G, Karunaratne TB, Frediani S, De Giorgio R. Chronic intestinal pseudo-obstruction: Progress in management? *Neurogastroenterol Motil*. 2017; 29(12).

30. Thapar N, Saliakellis E, Benninga MA, Borrelli O, Curry J, Faure C, De Giorgio R, Gupte G, Knowles CH, Staiano A, Vandenplas Y, Di Lorenzo C. Paediatric Intestinal Pseudo-obstruction: Evidence and Consensus-based Recommendations From an ESPGHAN-Led Expert Group. *J Pediatr Gastroenterol Nutr.* 2018; 66(6):991-1019.

31. Zenzeri L, Tambucci R, Quitadamo P, Giorgio V, De Giorgio R, Di Nardo G. Update on chronic intestinal pseudo-obstruction. *Curr Opin Gastroenterol*. 2020; 36(3):230-237.

32. Ziółkowska EA, Jansen MJ, Williams LL, Wang SH, Eultgen EM, Takahashi K, Le SQ, Nelvagal HR, Sharma J, Sardiello S, DeBosch BJ, Dickson PI, Anderson JB, Sax SE, Wright CM, Bradley RP, Whiteman IT, Makita T, Grider JR, Sands MS, Heuckeroth RO, Cooper JD. Gene therapy prevents bowel dysmotility, enteric neuron degeneration and extends survival in lysosomal storage disorder mouse models. *Sci Transl Med.* 2025; 17(781):eadj1445. doi: 10.1126/scitranslmed.adj1445.

33. Santavuori P, Linnankivi T, Jaeken J, Vanhanen SL, Telakivi T, Heiskala H. Psychological symptoms and sleep disturbances in neuronal ceroid-lipofuscinoses (NCL). *J Inher Metab Dis* 1993; 16:245-248.

34. Mannerkoski MK, Heiskala HJ, Santavuori PR, Pouttu JA. Transdermal fentanyl therapy for pains in children with infantile neuronal ceroid lipofuscinosis. *Eur J Paediatr Neurol*. 2001;5 Suppl A:175-7.

35. Barney CC, Hoch J, Byiers B, Dimian A, Symons FJ. A Case-controlled Investigation of Pain Experience and Sensory Function in Neuronal Ceroid Lipofuscinosis. *Clin J Pain*. 2015; 31(11):998-1003.

36. Ostergaard JR. Gait phenotype in Batten disease: A marker of disease progression. *Eur J Paediatr Neurol*. 2021; 35:1-7.

37. Yasa S, Butz ES, Colombo A, Chandrachud U, Montore L, Tschirner S, Prestel M, Sheridan SD, Müller SA, Groh J, Lichtenthaler SF, Tahirovic S, Cotman SL. Loss of CLN3 in microglia leads to impaired lipid metabolism and myelin turnover. *Commun Biol*. 2024; 7(1):1373.

38. Reed CB, Feltri ML, Wilson ER. Peripheral glia diversity. *J. Anat.* 2022; 241:1219–1234.

39. Salzer J, Feltri, ML, Jacob C. Schwann Cell Development and Myelination. *Cold Spring Harb. Perspect. Biol.* 2024; 16:a041360.

40. Taveggia, C. Schwann cells-axon interaction in myelination. *Curr. Opin. Neurobiol.* 2016; 39: 24–29.

41. Bosch-Queralt M, Fledrich R, Stassart RM. Schwann cell functions in peripheral nerve development and repair. *Neurobiol Dis*. 2023; 176:105952.

42. Hastings RL, Valdez G. Origin, identity, and function of terminal Schwann cells. *Trends Neurosci*. 2024; 47(6):432-446.

43. Santosa KB, Keane AM, Jablonka-Shariff A, Vannucci B, Snyder-Warwick AK. Clinical relevance of terminal Schwann cells: an overlooked component of the neuromuscular junction. *J Neurosci Res*. 2018; 96(7):1125-1135.

44. Sands MS, Davidson BL. Gene therapy for lysosomal storage diseases. *Mol Ther*. 2006; 13(5):839-49.

45. Sondhi D, Scott EC, Chen A, Hackett NR, Wong AM, Kubiak A, Nelvagal HR, Pearse Y, Cotman SL, Cooper JD, Crystal RG. Partial correction of the CNS lysosomal storage defect in a mouse model of juvenile neuronal ceroid lipofuscinosis by neonatal CNS administration of an adeno-associated virus serotype rh.10 vector expressing the human CLN3 gene. *Hum Gene Ther*. 2014; 25(3):223-39.

46. Bosch ME, Aldrich A, Fallet R, Odvody J, Burkovetskaya M, Schuberth K, Fitzgerald JA, Foust KD, Kielian T. Self-Complementary AAV9 Gene Delivery Partially Corrects Pathology Associated with Juvenile Neuronal Ceroid Lipofuscinosis (CLN3). *J Neurosci*. 2016; 36(37):9669-82.

47. Johnson TB, Brudvig JJ, Likhite S, Pratt MA, White KA, Cain JT, Booth CD, Timm DJ, Davis SS, Meyerink B, Pineda R, Dennys-Rivers C, Kaspar BK, Meyer K, Weimer JM. Early postnatal administration of an AAV9 gene therapy is safe and efficacious in CLN3 disease. *Front Genet*. 2023; 14:1118649. doi: 10.3389/fgene.2023.1118649.

48. Avetisyan M, Wang H, Schill EM, Bery S, Grider JR, Hassell JA, Stappenbeck T, Heuckeroth RO. Hepatocyte Growth Factor and MET Support Mouse Enteric Nervous System Development, the Peristaltic Response, and Intestinal Epithelial Proliferation in Response to Injury. *J Neurosci*. 2015; 35(33):11543-58.

49. Schill EM, Wright CM, Jamil A, LaCombe JM, Roper RJ, Heuckeroth RO. Down syndrome mouse models have an abnormal enteric nervous system. *JCI Insight*. 2019; 5(11):e124510.

50. Wright CM, Garifallou JP, Schneider S, Mentch HL, Kothakapa DR, Maguire BA, Heuckeroth RO. Dlx1/2 mice have abnormal enteric nervous system function. *JCI Insight*. 2020; 5(4):e131494.

51. Rao M, Nelms BD, Dong L, Salinas-Rios V, Rutlin M, Gershon MD, Corfas G. Enteric glia express proteolipid protein 1 and are a transcriptionally unique population of glia in the mammalian nervous system. *Glia* 2015; 63: 2040–2057 (2015).

52. Muller PA, Koscsó B, Rajani GM, Stevanovic K, Berres ML, Hashimoto D, Mortha A, Leboeuf M, Li XM, Mucida D, Stanley ER, Dahan S, Margolis KG, Gershon MD, Merad M, Bogunovic M. Crosstalk between Muscularis Macrophages and Enteric Neurons Regulates Gastrointestinal Motility. *Cell*. 2014; 158(5):1210.

53. Stakenborg M, Abdurahiman S, De Simone V, Goverse G, Stakenborg N, van Baarle L, Wu Q, Pirottin D, Kim JS, Chappell-Maor L, Pintelon I, Thys S, Pollenus E, Boon L, Van den Steen P, Hao M, Van Ginderachter JA, Boeckxstaens GE, Timmermans JP, Jung S, Marichal T, Ibiza S, Matteoli G. Enteric glial cells favor accumulation of anti-inflammatory macrophages during the resolution of muscularis inflammation. *Mucosal Immunol*. 2022; 15(6):1296-1308.

54. Graham KD, López SH, Sengupta R, Shenoy A, Schneider S, Wright CM, Feldman M, Furth E, Valdivieso F, Lemke A, Wilkins BJ, Naji A, Doolin EJ, Howard MJ, Heuckeroth RO. Robust, 3-

Dimensional Visualization of Human Colon Enteric Nervous System Without Tissue Sectioning. *Gastroenterology*. 2020; 158(8):2221-2235.e5. doi: 10.1053/j.gastro.2020.02.035

55. Heuckeroth RO, López SH, Graham KD, Sengupta R. Human colon tissue clearing and immunohistochemistry (protocols.io, 2020); https://doi.org/10.17504/protocols.io.wyeffte

56. Eisenberg JD, Bradley RP, Graham KD, Ceron RH, Lemke AM, Wilkins BJ, Naji A, Heuckeroth RO. Three-Dimensional Imaging of the Enteric Nervous System in Human Pediatric Colon Reveals New Features of Hirschsprung's Disease. *Gastroenterology*. 2024; 167(3):547-559.

57. Hunter DA, Pan D, Wood MD, Snyder-Warwick AK, Moore AM, Feldman EL, Mackinnon SE, Brenner MJ. Design-Based stereology and binary image histomorphometry in nerve assessment. *J Neurosci Methods*. 2020; 336:108635.

58. Hunter DA, Moradzadeh A, Whitlock EL, Brenner MJ, Myckatyn TM, Wei CH, Tung TH, Mackinnon SE. Binary imaging analysis for comprehensive quantitative histomorphometry of peripheral nerve. *J Neurosci Methods*. 2007; 166(1):116-24.

59. Donsante A, Miller DG, Li Y, Vogler C, Brunt EM, Russell DW, Sands MS. AAV vector integration sites in mouse hepatocellular carcinoma. *Science*. 2007; 317(5837):477.

60. Sabatino DE, Bushman FD, Chandler RJ, Crystal RG, Davidson BL, Dolmetsch R, Eggan KC, Gao G, Gil-Farina I, Kay MA, McCarty DM, Montini E, Ndu A, Yuan J; American Society of Gene and Cell Therapy (ASGCT) Working Group on AAV Integration. Evaluating the state of the science for adeno-associated virus integration: An integrated perspective. *Mol Ther*. 2022; 30(8):2646-2663.

61. Ostergaard JR, Rasmussen TB, Mølgaard H. Neurology. Cardiac involvement in juvenile neuronal ceroid lipofuscinosis (Batten disease). *Neurology* 2011; 76(14):1245-51.

62. Rietdorf K, Coode EE, Schulz A, Wibbeler E, Bootman MD, Ostergaard JR. Cardiac pathology in neuronal ceroid lipofuscinoses (NCL): More than a mere co-morbidity. *Biochim Biophys Acta Mol Basis Dis*. 2020; 1866(9):165643.

63. Ostergaard JR. Etiology of anxious and fearful behavior in juvenile neuronal ceroid lipofuscinosis (CLN3 disease). *Front Psychiatry*. 2023; 14:1059082.

64. Ostergaard JR. Treatment of non-epileptic episodes of anxious, fearful behavior in adolescent juvenile neuronal ceroid lipofuscinosis (CLN3 disease). *Front Neurol*. 2023; 14:1216861.

65. Baekmann C, Handrup MM, Molgaard H, Ejerskov C, Jensen HK, Ostergaard JR. Insight of autonomic dysfunction in CLN3 disease: a study on episodes resembling paroxysmal sympathetic hyperactivity (PSH). *Orphanet J Rare Dis*. 2024; 19(1):374.

66. Cooper JD, Tarczyluk MA, Nelvagal HR. Towards a new understanding of NCL pathogenesis. *Biochim Biophys Acta*. 2015; 1852(10 Pt B):2256-61.

67. Nelvagal HR, Lange J, Takahashi K, Tarczyluk-Wells MA, Cooper JD. Pathomechanisms in the neuronal ceroid lipofuscinoses. *Biochim Biophys Acta Mol Basis Dis*. 2020; 1866(9):165570.

68. Lim MJ, Alexander N, Benedict JW, Chattopadhyay S, Shemilt SJ, Guérin CJ, Cooper JD, Pearce DA. IgG entry and deposition are components of the neuroimmune response in Batten disease. *Neurobiol Dis*. 2007; 25(2):239-51.

69. Seehafer SS, Ramirez-Montealegre D, Wong AM, Chan CH, Castaneda J, Horak M, Ahmadi SM, Lim MJ, Cooper JD, Pearce DA. Immunosuppression alters disease severity in juvenile Batten disease mice. *J Neuroimmunol*. 2011; 230(1-2):169-72.

70. Kovács AD, Saje A, Wong A, Szénási G, Kiricsi P, Szabó E, Cooper JD, Pearce DA. Temporary inhibition of AMPA receptors induces a prolonged improvement of motor performance in a mouse model of juvenile Batten disease. *Neuropharmacology*. 2011; 60(2-3):405-9.

71. Kovács AD, Saje A, Wong A, Ramji S, Cooper JD, Pearce DA. Age-dependent therapeutic effect of memantine in a mouse model of juvenile Batten disease. *Neuropharmacology*. 2012; 63(5):769-75.

72. Aldrich A, Bosch ME, Fallet R, Odvody J, Burkovetskaya M, Rama Rao KV, Cooper JD, Drack AV, Kielian T. Efficacy of phosphodiesterase-4 inhibitors in juvenile Batten disease (CLN3). *Ann Neurol.* 2016; 80(6):909-923.

73. Palmieri M, Pal R, Nelvagal HR, Lotfi P, Stinnett GR, Seymour ML, Chaudhury A, Bajaj L, Bondar VV, Bremner L, Saleem U, Tse DY, Sanagasetti D, Wu SM, Neilson JR, Pereira FA, Pautler RG, Rodney GG, Cooper JD, Sardiello M. mTORC1-independent TFEB activation via Akt inhibition promotes cellular clearance in neurodegenerative storage diseases. *Nat Commun*. 2017; 8:14338.

74. Tarczyluk-Wells MA, Salzlechner C, Najafi AR, Lim MJ, Smith D, Platt FM, Williams BP, Cooper JD. Combined Anti-inflammatory and Neuroprotective Treatments Have the Potential to Impact Disease Phenotypes in *Cln3*$^{-/-}$ Mice. *Front Neurol*. 2019; 10:963.

75. Handrup MM, Mølgaard H, Andersen BN, Ostergaard JR. Pacemaker Implantation in Juvenile Neuronal Ceroid Lipofuscinosis (CLN3)-A Long-Term Follow-Up Study. *Front Neurol*. 2022; 13:846240.

76. Lovering RM, Iyer SR, Edwards B, Davies KE. Alterations of neuromuscular junctions in Duchenne muscular dystrophy. *Neurosci Lett*. 2020; 737:135304.

77. Ng SY, Ljubicic V. Recent insights into neuromuscular junction biology in Duchenne muscular dystrophy: Impacts, challenges, and opportunities. *EBioMedicine*. 2020; 61:103032.

78. Falk DJ, Todd AG, Lee S, Soustek MS, ElMallah MK, Fuller DD, Notterpek L, Byrne BJ. Peripheral nerve and neuromuscular junction pathology in Pompe disease. *Hum Mol Genet*. 2015; 24(3):625-36.

79. Rapola J, Haltia M. Cytoplasmic inclusions in the vermiform appendix and skeletal muscle in two types of so-called neuronal ceroid-lipofuscinosis. *Brain*. 1973; 96(4):833-40.

80. Levine AS, Lemieux B, Brunning R, White JG, Sharp HL, Stadlan E, Krivit W. Ceroid accumulation in a patient with progressive neurological disease. *Pediatrics*. 1968; 42(3):583-91.

81. Ryan GB, Anderson M, Menkes JH, Dennett X. Lipofuscin (ceroid) storage disease of the brain neuropathological and neurochemical studies. *Brain*. 1970; 93(3):617-28.

82. Radke J, Koll R, Gill E, Wiese L, Schulz A, Kohlschütter A, Schuelke M, Hagel C, Stenzel W, Goebel HH. Autophagic vacuolar myopathy is a common feature of CLN3 disease**.** *Ann Clin Transl Neurol*. 2018; 5(11):1385-1393.

83. Moro F, Rubegni A, Pochiero F, Mero S, Procopio E, Baldacci J, Donati MA, Santorelli FM. Autophagic vacuolar myopathy caused by a CLN3 mutation. A case report. *Neuromuscul Disord*. 2019; 29(1):67-69.

84. Haltia M, Rapola J, Santavuori P, Keränen A. Infantile type of so-called neuronal ceroid-lipofuscinosis. 2. Morphological and biochemical studies. *J Neurol Sci.* 1973; 18(3):269-85.

85. Haltia M, Rapola J, Santavuori P. Infantile type of so-called neuronal ceroid-lipofuscinosis. Histological and electron microscopic studies. *Acta Neuropathol.* 1973; 26(2):157-70.

86. Todd AG, McElroy JA, Grange RW, Fuller DD, Walter GA, Byrne BJ, Falk DJ. Correcting Neuromuscular Deficits With Gene Therapy in Pompe Disease. *Ann Neurol*. 2015; 78(2):222-34.

87. Cotman SL, Vrbanac V, Lebel LA, Lee RL, Johnson KA, Donahue LR, Teed AM, Antonellis K, Bronson RT, Lerner TJ, MacDonald ME. Cln3(Deltaex7/8) knock-in mice with the common JNCL mutation exhibit progressive neurologic disease that begins before birth. *Hum Mol Genet*. 2002; 11(22):2709-21.

88. Snyder-Warwick AK, Satoh A, Santosa KB, Imai SI, Jablonka-Shariff A. Hypothalamic Sirt1 protects terminal Schwann cells and neuromuscular junctions from age-related morphological changes. *Aging Cell*. 2018; e12776. doi: 10.1111/acel.12776.

89. Griffey MA, Bible E, Vogler C, Levy B, Gupta P, Cooper JD, Sands MS. Adeno-associated virus 2-mediated gene therapy decreases autofluorescent storage material and increases brain mass in a murine model of infantile neuronal ceroid lipofuscinosis. *Neurobiol Dis.* 2004; 16(2):360-69.

90. Griffey M, Macauley SL, Ogilvie JM, Sands MS. AAV2-mediated ocular gene therapy for infantile neuronal ceroid lipofuscinosis. *Mol Ther.* 2005; 12(3):413-21.

91. Griffey MA, Wozniak D, Wong M, Bible E, Johnson K, Rothman SM, Wentz AE, Cooper JD, Sands MS. CNS-directed AAV2-mediated gene therapy ameliorates functional deficits in a murine model of infantile neuronal ceroid lipofuscinosis *Mol Ther.* 2006; 13(3):538-47.

92. Macauley SL, Roberts MS, Wong AM, McSloy F, Reddy AS, Cooper JD, Sands MS. Synergistic effects of central nervous system-directed gene therapy and bone marrow transplantation in the murine model of infantile neuronal ceroid lipofuscinosis. *Ann Neurol*. 2012; 71(6):797-804.

93. Roberts MS, Macauley SL, Wong AM, Yilmas D, Hohm S, Cooper JD, Sands MS. Combination small molecule PPT1 mimetic and CNS-directed gene therapy as a treatment for infantile neuronal ceroid lipofuscinosis. *J Inherit Metab Dis.* 2012; 35(5):847-57.

94. Macauley SL, Wong AM, Shyng C, Augner DP, Dearborn JT, Pearse Y, Roberts MS, Fowler SC, Cooper JD, Watterson DM, Sands MS. An anti-neuroinflammatory that targets dysregulated glia enhances the efficacy of CNS-directed gene therapy in murine infantile neuronal ceroid lipofuscinosis. *J Neurosci*. 2014; 34(39):13077-82.

95. Shyng C, Nelvagal HR, Dearborn JT, Tyynelä J, Schmidt RE, Sands MS, Cooper JD. Synergistic effects of treating the spinal cord and brain in CLN1 disease. *Proc Natl Acad Sci U S A*. 2017; 114(29):E5920-E5929.

Figure 1

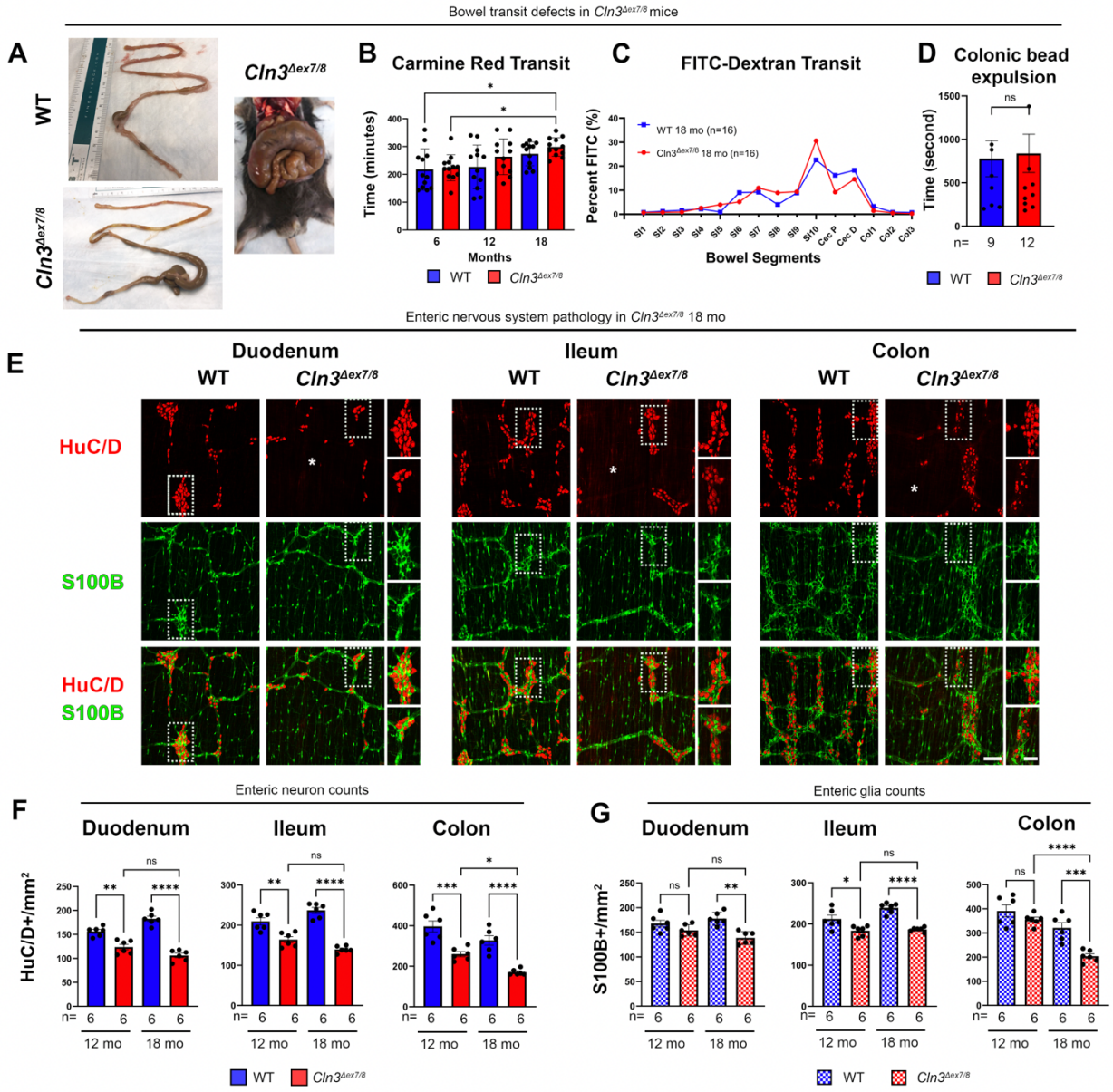

Fig. 1 Enteric nervous system pathology in *Cln3*$^{\Delta ex7/8}$ mice. (A) *Cln3*$^{\Delta ex7/8}$ mice display distention of the small intestine and cecum by fecal material at disease end-stage. **(B,C,D)** Bowel transit was assessed by measuring the time for gavaged carmine red to appear in stool **(B)** or determining the amount of FITC conjugated dextrans present in individual bowel segments 2 hours after gavage **(C)** (SI1-SI10 = numbered segments of small intestine; Cec P=proximal cecum; Cec D=distal cecum; Col1-Col3=numbered segments of colon). **(D)** Time taken to expel a glass bead

from the colon was measured at disease endstage. **(E)** Whole-mount bowel preparations immunostained for pan-neuronal marker HuC/D (red) and glial marker S100B (green) reveal the loss of myenteric plexus neurons and changes in their neuron morphology in the duodenum, ileum and colon of disease endstage *Cln3*$^{\Delta ex7/8}$ mice vs. age matched wildtype (WT) controls at 18 months (mo). Scale bar 200µm, 100µm inserts, respectively. Asterix (*) indicates regions of near complete enteric neuron loss**. (F, G)** The density of HuC/D+ neurons and S100B+ enteric glia was measured in these mice at endstage. Data ± SEM (B, D, F). One-way ANOVA with a post-hoc Bonferroni correction **(B, C, D, F, G)**, * $p \leq 0.05$, ** $p \leq 0.01$, *** $p \leq 0.001$, **** $p \leq 0.0001$, ns = not significant.

Figure 2

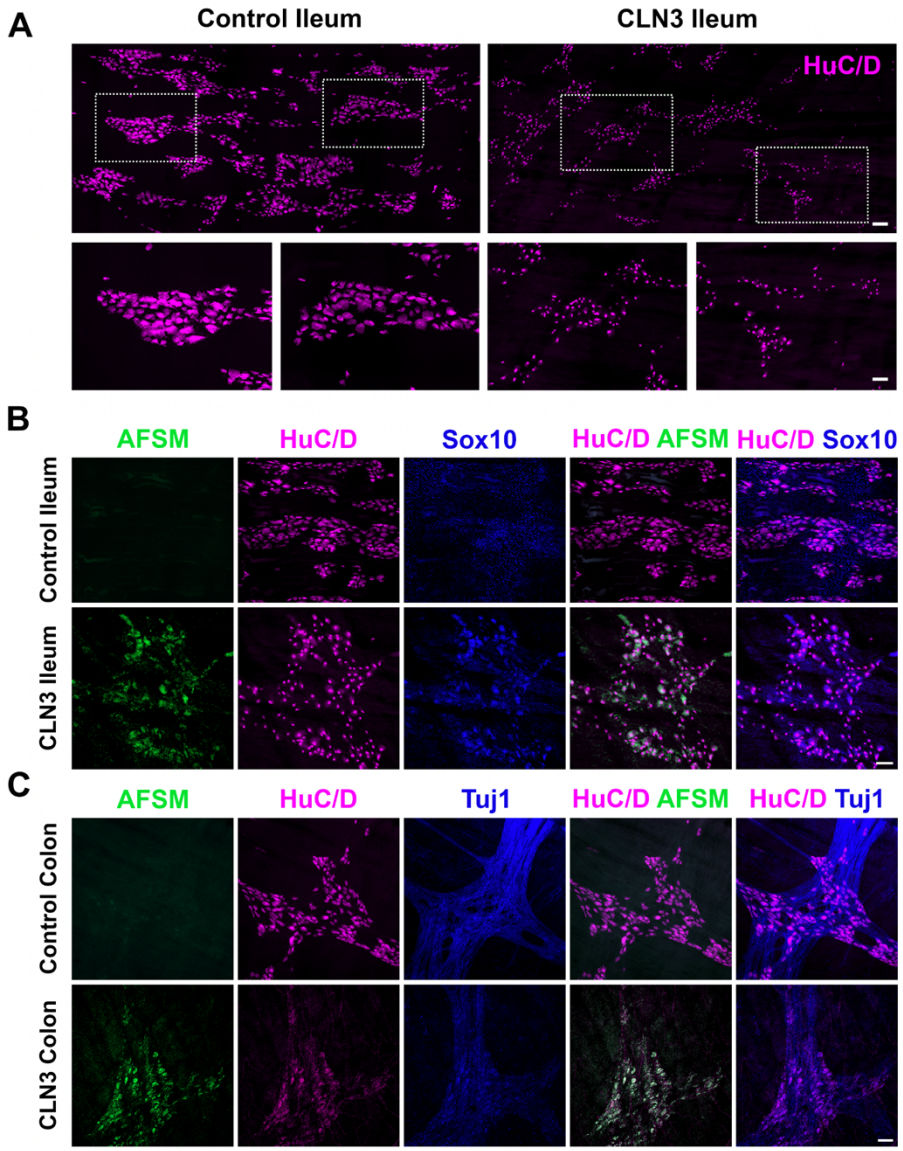

Fig. 2 Enteric nervous system pathology in a human bowel from a young adult with CLN3 disease. (**A**) Human ileum from a previously healthy 17-year-old (left) and an ileum from a 21-year-old young adult who died from CLN3 disease (right) was stained with antibodies to pan-neuronal protein HuC/D (magenta), cleared, and imaged by confocal microscopy from mucosa to serosa with a 10X objective. Large images show stitched confocal Z-stacks of layers containing myenteric plexus. Scale bar = 1000 μm. Lower panels are magnifications of the regions enclosed

in boxes from large tiled images in the top row. Scale bar = 100 μm. (**B**) Ileum from the same healthy 17-year-old and the same child with CLN3 disease was stained with antibodies to HuC/D (magenta) and SOX10 (blue), cleared and imaged by confocal microscopy from mucosa to serosa with a 10X objective. Images show autofluorescent storage material (AFSM, green), HuC/D and SOX10 signals a single slice from the confocal Z-stack in the layer containing myenteric plexus. Scale bar = 100 μm. (**C**) Colon from a previously healthy 18-year-old organ donor and the same child with CLN3 disease was stained with antibodies to HuC/D (magenta) and Tuj1 (blue), cleared and imaged by confocal microscopy from mucosa to serosa with a 10X objective. Images show AFSM, HuC/D and Tuj1 signals a single slice from the confocal Z-stack in the layer containing myenteric plexus. Scale bar = 100 μm.

Figure 3

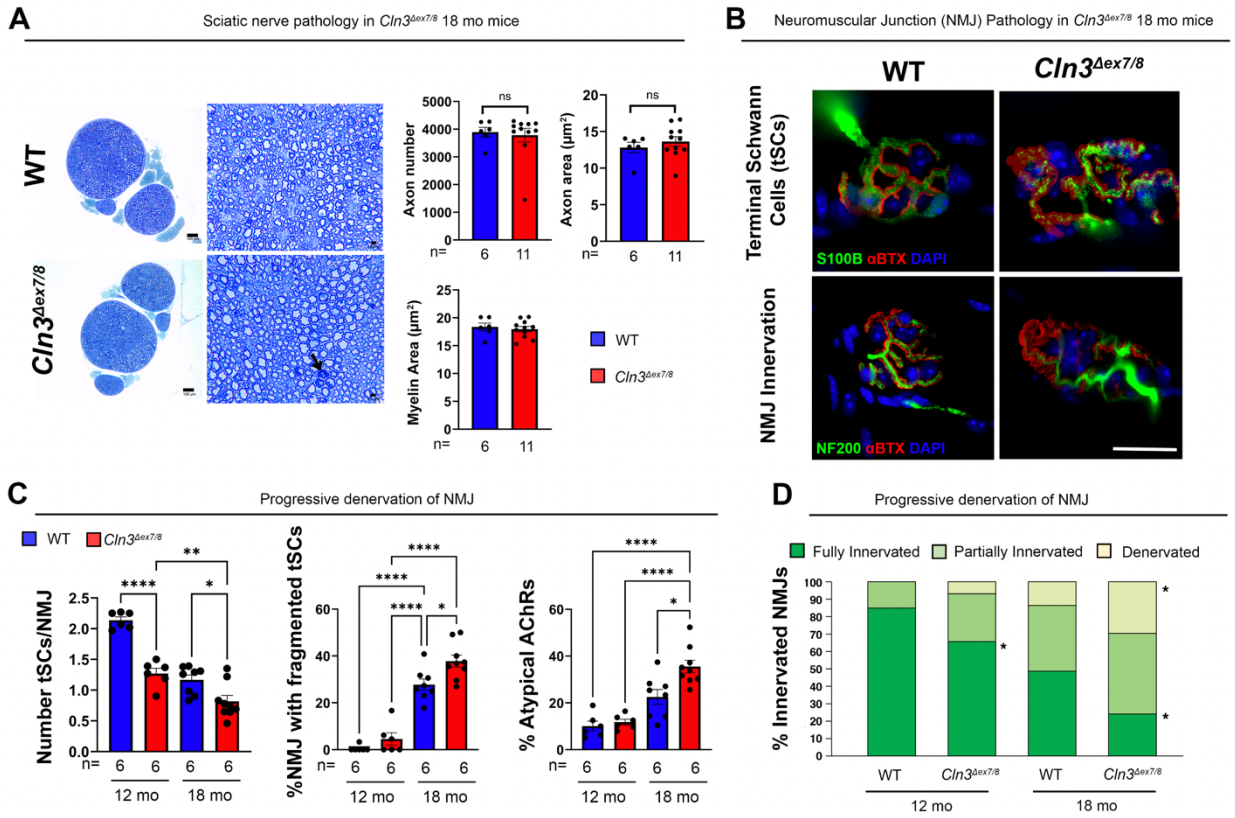

Fig. 3 Sciatic nerve and neuromuscular junction (NMJ) pathology in *Cln3*$^{\Delta ex7/8}$ mice. (A) Semi-thin (1 μm) sections of the sciatic nerve stained with toluidine blue show no significant (ns) differences in the number of axon, axon area or myelin area in 18 months (mo) *Cln3*$^{\Delta ex7/8}$ mice vs. age matched wildtype (WT) controls. Arrow indicates an area of vacuolation. Scale bar 100μm for lower power view; 1μm for higher power view. Histograms show measurements of axon number, axon area and myelin area made from sciatic nerve sections. **(B)** Representative images of NMJ morphology in the extensor digitorum longus (EDL) muscle. Immunofluorescence staining for acetylcholine receptors (αBTX = α-bungarotoxin for AChRs; red), terminal Schwann cells (tSCs, S100B; green), and neurofilament (NF200; green) shows altered NMJ innervation patterns in *Cln3*$^{\Delta ex7/8}$ mice, with fragmented Schwann cell coverage. Scale bar 20μm. **(C)** Quantification reveals a significant reduction in the number of tSCs, an increase in NMJs with fragmented tSCs

and atypical AChRs in *Cln3*$^{\Delta ex7/8}$ mice vs. age WT at 12 and 18 months. **(D)** *Cln3*$^{\Delta ex7/8}$ mice show a progressive loss of fully innervated NMJs compered to age matched WT mice. NMJs were defined as fully innervated if nerve occupied ≥ 75% of endplate area. NMJ percentages were normalized to the total NMJ number in the microscopic field of view. Data ± SEM. One-way ANOVA with a post-hoc Bonferroni correction (**A, C, D**), * $p \leq 0.05$, ** $p \leq 0.01$, *** $p \leq 0.001$, **** $p \leq 0.0001$, ns = not significant.

Figure 4

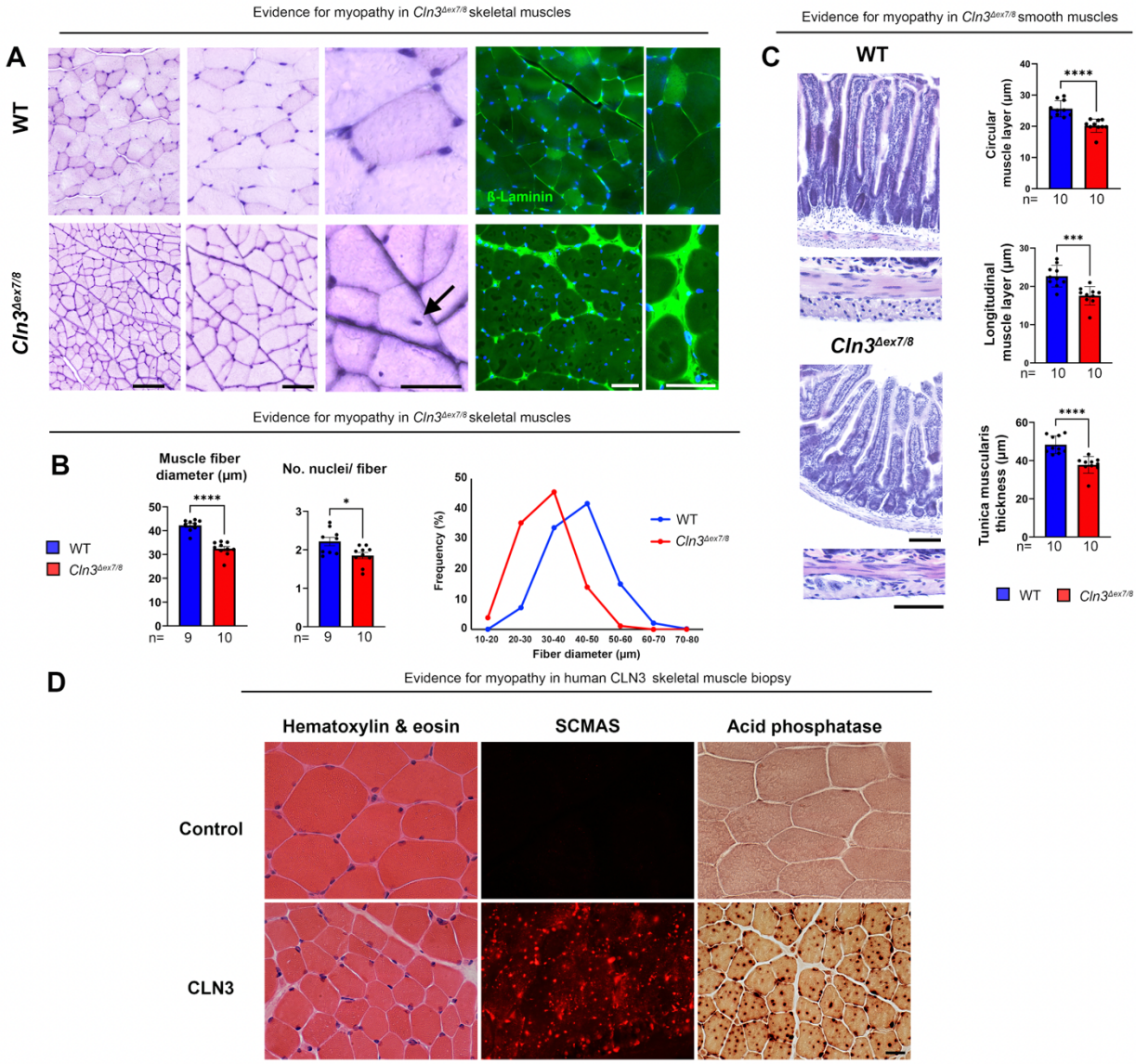

Fig. 4 Evidence for myopathy in skeletal and smooth muscles in *Cln3$^{\Delta ex7/8}$* mice and in a human CLN3 muscle biopsy sample. (A) Hematoxylin and eosin staining reveals the histopathological changes in *Cln3$^{\Delta ex7/8}$* quadriceps muscle compared to age matched WT controls at 18 months. Changes were also pronounced in extracellular deposit of ß-laminin (green) between myofibers in *Cln3$^{\Delta ex7/8}$* mice vs WT at 18 months of age. Scale bar 100µm, 50µm in inserts. **(B)** The muscle fiber diameter and number of nuclei per myofiber was measured in the

quadriceps muscles at disease endstage. **(C)** Evidence for myopathy in smooth muscles was analyzed in jejunum *Cln3*$^{\Delta ex7/8}$ mice vs WT at 18 months. Scale bar 200μm (full thickness sections), 50μm in inserts (closer view of smooth muscle layers). Unpaired t-test (B,C), * $p \leq 0.05$, ** $p \leq 0.01$, *** $p \leq 0.001$, **** $p \leq 0.0001$. (**D**) Hematoxylin and eosin staining reveals evidence for myopathy in a human CLN3 quadriceps muscle biopsy, with accumulation of both subunit c of mitochondrial ATP synthetase (SCMAS) immunoreactivity and acid phosphatase positive inclusions. Scale bar 50μm. Data ± SEM.

Figure 5

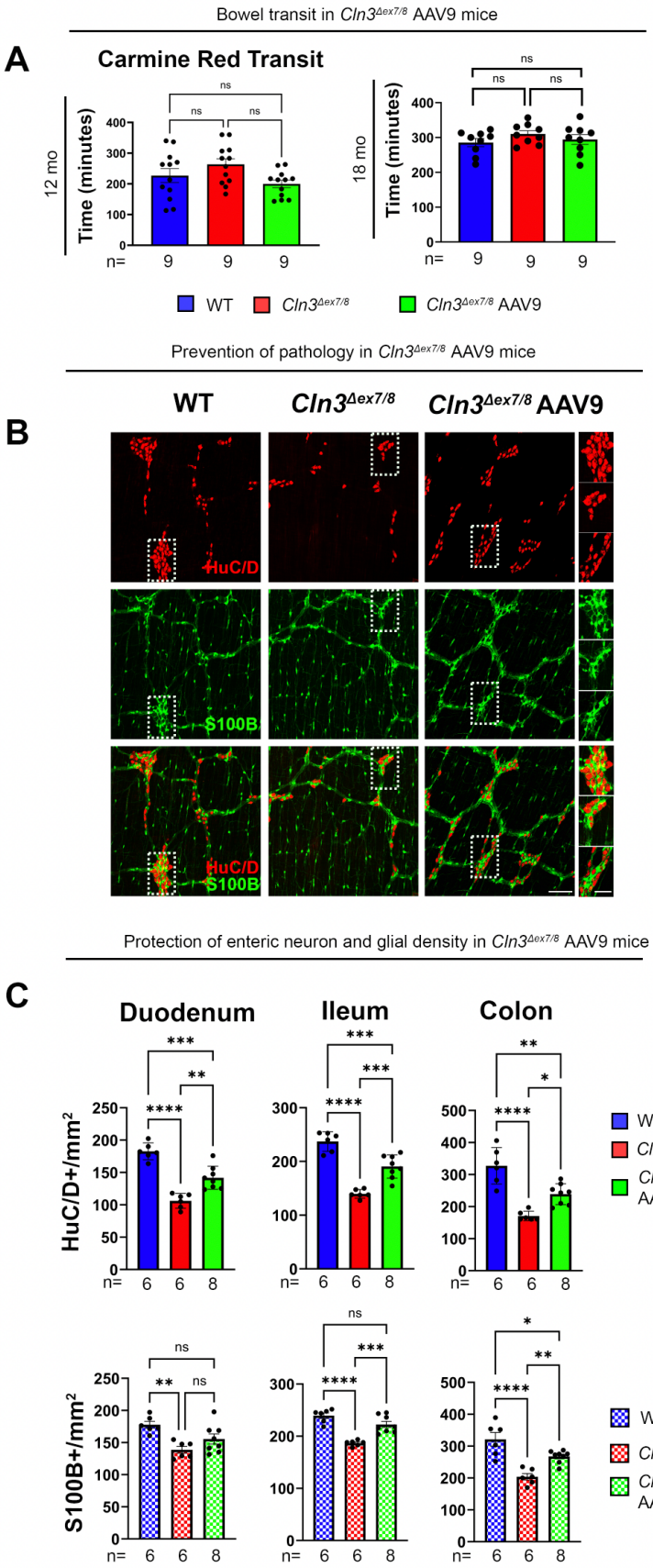
Bowel transit in Cln3Δex7/8 AAV9 mice
A
Carmine Red Transit
12 mo
Time (minutes)
ns
ns
ns
n= 9 9 9
18 mo
Time (minutes)
ns
ns
ns
n= 9 9 9
WT
Cln3Δex7/8
Cln3Δex7/8 AAV9
Prevention of pathology in Cln3Δex7/8 AAV9 mice
B
WT
Cln3Δex7/8
Cln3Δex7/8 AAV9
HuC/D
S100B
HuC/D
S100B
Protection of enteric neuron and glial density in Cln3Δex7/8 AAV9 mice
C
Duodenum
Ileum
Colon
HuC/D+/mm2
S100B+/mm2
n= 6 6 8
WT
Cln3Δex7/8
Cln3Δex7/8 AAV9

Fig. 5 Effects of gene therapy upon the bowel of *Cln3*$^{\Delta ex7/8}$ mice. (A) Total bowel transit was compared at 12 and 18 months (mo) in untreated *Cln3*$^{\Delta ex7/8}$ mice, *Cln3*$^{\Delta ex7/8}$ mice treated with AAV9-hCLN3 as neonates (P1) and age-matched wildtype (WT) controls. This was done by measuring the time for gavaged Carmine red to appear in stool. **(B)** Representative photomicrographs of whole-mount bowel preparations of the ileum immunostained for the pan-neuronal marker HuC/D (red) and S100B (green) reveal the protective effects of neonatal intravenous AAV9-hCLN3 treatment upon myenteric plexus neurons in the bowel of disease endstage *Cln3*$^{\Delta ex7/8}$ mice treated at P1 vs. WT controls at 18 months. Scale bar 200μm, 50 μm higher power views. (**C**) Measurements of the density of HuC/D positive neurons and glia reveal more neurons present in all bowel regions of 18-month-old *Cln3*$^{\Delta ex7/8}$ mice treated neonatally with AAV9-hCLN3. One-way ANOVA with a post-hoc Bonferroni correction **(A, C)**, * $p \leq 0.05$, ** $p \leq 0.01$, *** $p \leq 0.001$, **** $p \leq 0.0001$. Data ± SEM.

Figure 6

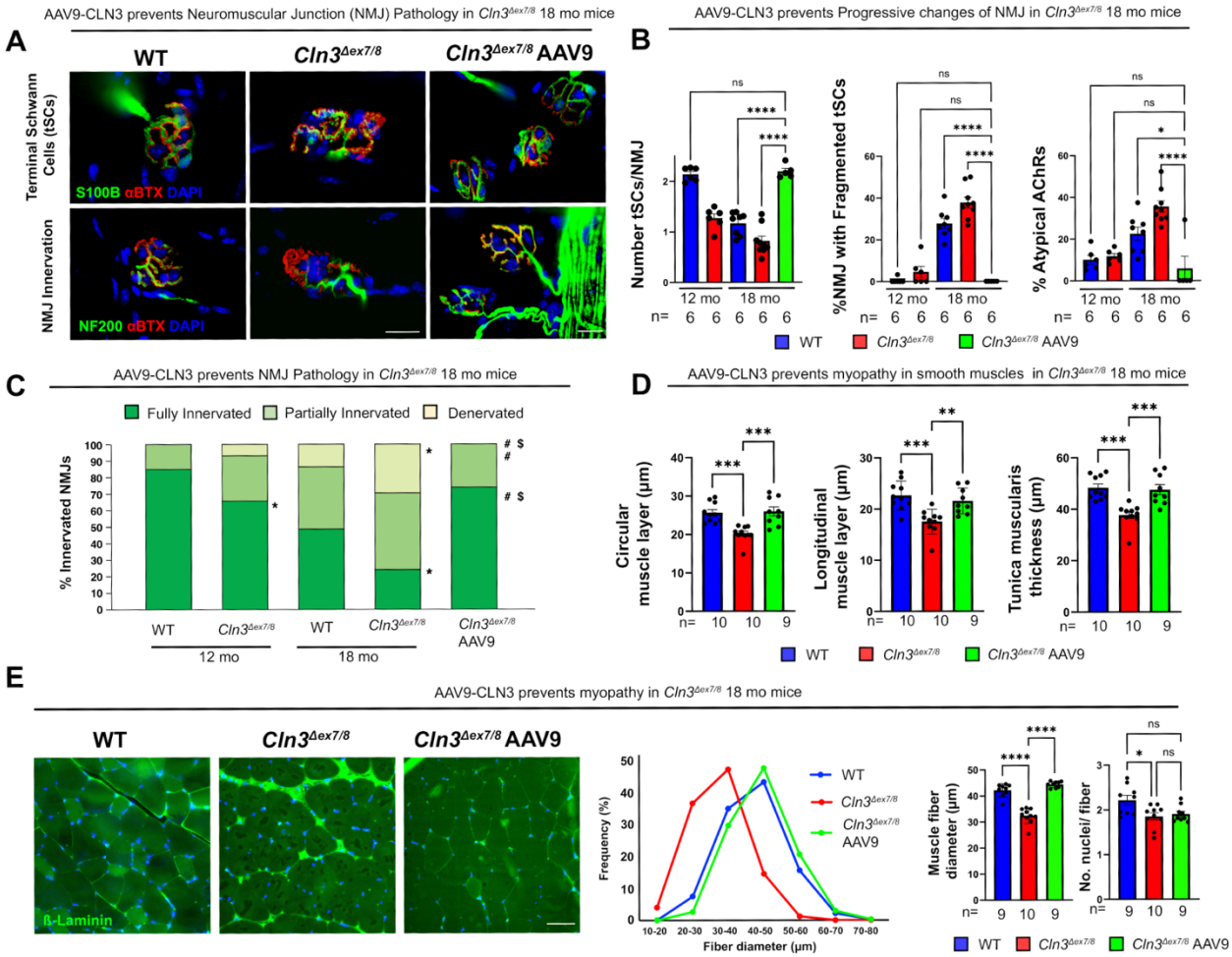

Fig 6. Treatment effect of gene therapy upon neuromuscular junction pathology and myopathy in *Cln3*$^{\Delta ex7/8}$ mice at 18 months. (A) Representative images of NMJ morphology in the extensor digitorum longus (EDL) muscle in untreated *Cln3*$^{\Delta ex7/8}$ mice, *Cln3*$^{\Delta ex7/8}$ mice treated with AAV9-hCLN3 and age matched WT. Immunofluorescence staining for acetylcholine receptors (αBTX= α-bungarotoxin for AChRs; red), terminal Schwann cells (tSCs, S100B; green), and neurofilament (NF200; green), with DAPI nuclear staining (blue). Scale bar 20µm. **(B)** Quantification of NMJs shows the protective effect of gene therapy upon the number of tSCs per NMJ, a decreased proportion of NMJs with fragmented tSCs and atypical AChRs. **(C)** Analysis showed an increase in fully innervated NMJs in *Cln3*$^{\Delta ex7/8}$ mice treated with AAV9-hCLN3 at 18

months compared to untreated *Cln3*$^{\Delta ex7/8}$ mice and WT mice at 18 months. NMJs were defined as fully innervated if nerve occupied ≥ 75% of endplate area. NMJ percentages were normalized to the total NMJ number in the microscopic field of view. Data ± SEM. * *Cln3*$^{\Delta ex7/8}$ vs. WT; $^{\#}$ AAV9-hCLN3 vs. *Cln3*$^{\Delta ex7/8}$; $^{\$}$ AAV9-hCLN3 vs. WT. Scale bar 20 µm. **(D)** AAV9 gene therapy prevents thinning of bowel smooth muscle in the jejenum of *Cln3*$^{\Delta ex7/8}$ mice at 18 months of age. **(E)** Analysis of quadriceps muscle shows less deposition of ß-laminin between myofibrils in AAV9-hCLN3 treated *Cln3*$^{\Delta ex7/8}$ mice than in untreated *Cln3*$^{\Delta ex7/8}$ mice. This treatment also prevented the reduction in muscle fiber diameter (histogram of average diameter and size-distribution line graph), while the average number of nuclei per myofiber remained significantly less than in WT mice. Scale bar 50 µm. One-way ANOVA with a post-hoc Bonferroni correction **(B, C, D, E)**, * $p \leq 0.05$, ** $p \leq 0.01$, *** $p \leq 0.001$, **** $p \leq 0.0001$.

Supplementary Figure 1

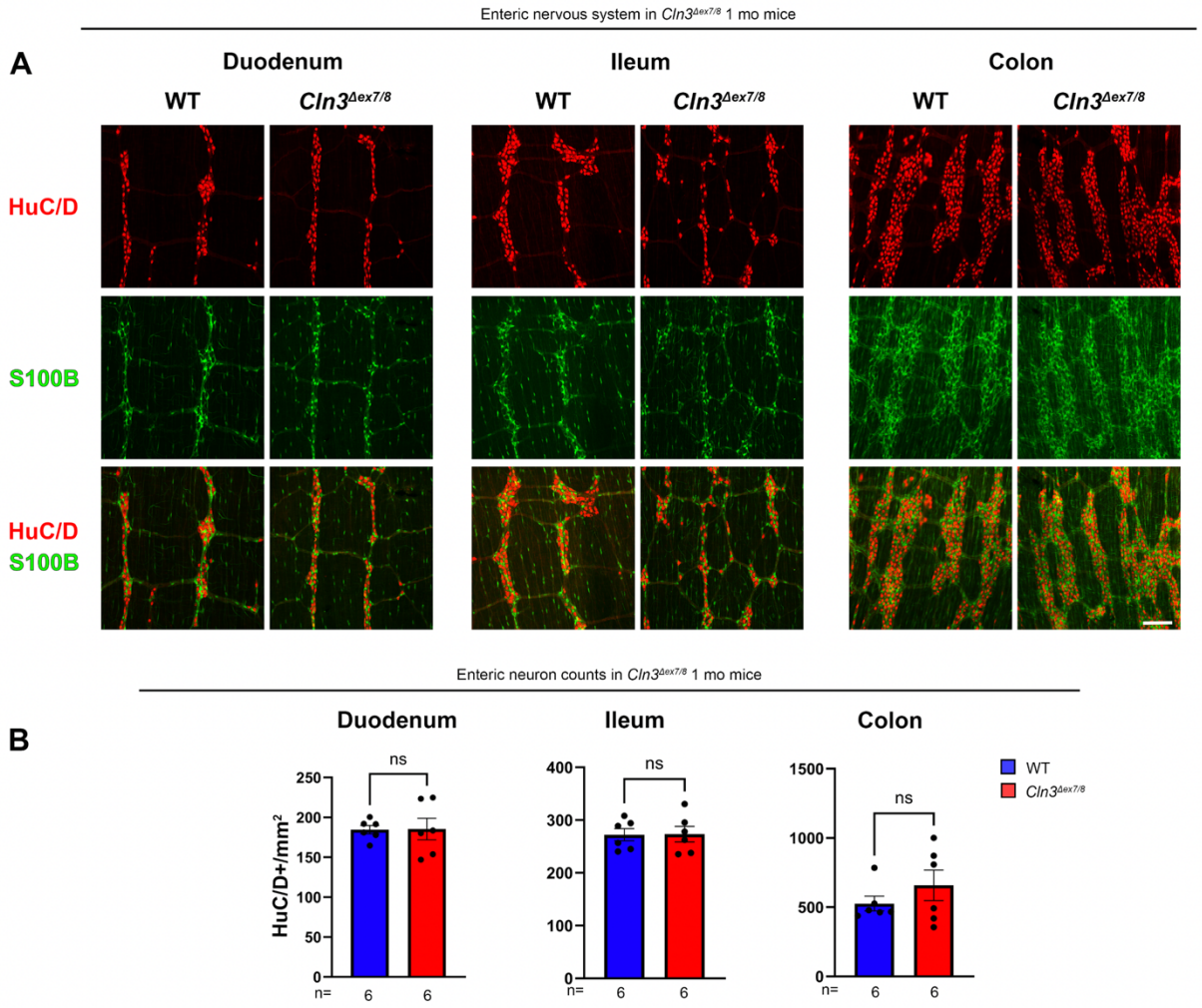

Fig. S1. Lack of readily detectable enteric nervous system pathology. (A) Merged images showing immunostaining for HuC/D (neurons, red) and the glial marker S100B (green) reveal the myenteric plexus of 1 month old *Cln3*$^{\Delta ex7/8}$ mice appears similar to age matched WT mice. Scale bar 200μm. **(B)** Counts of the density of HuC/D+ neurons reveal no significant difference in any bowel regions of 1 month old *Cln3*$^{\Delta ex7/8}$ mice compared to age matched WT controls. Unpaired t-test **(B)**. Data ± SEM.

Supplementary Figure 2

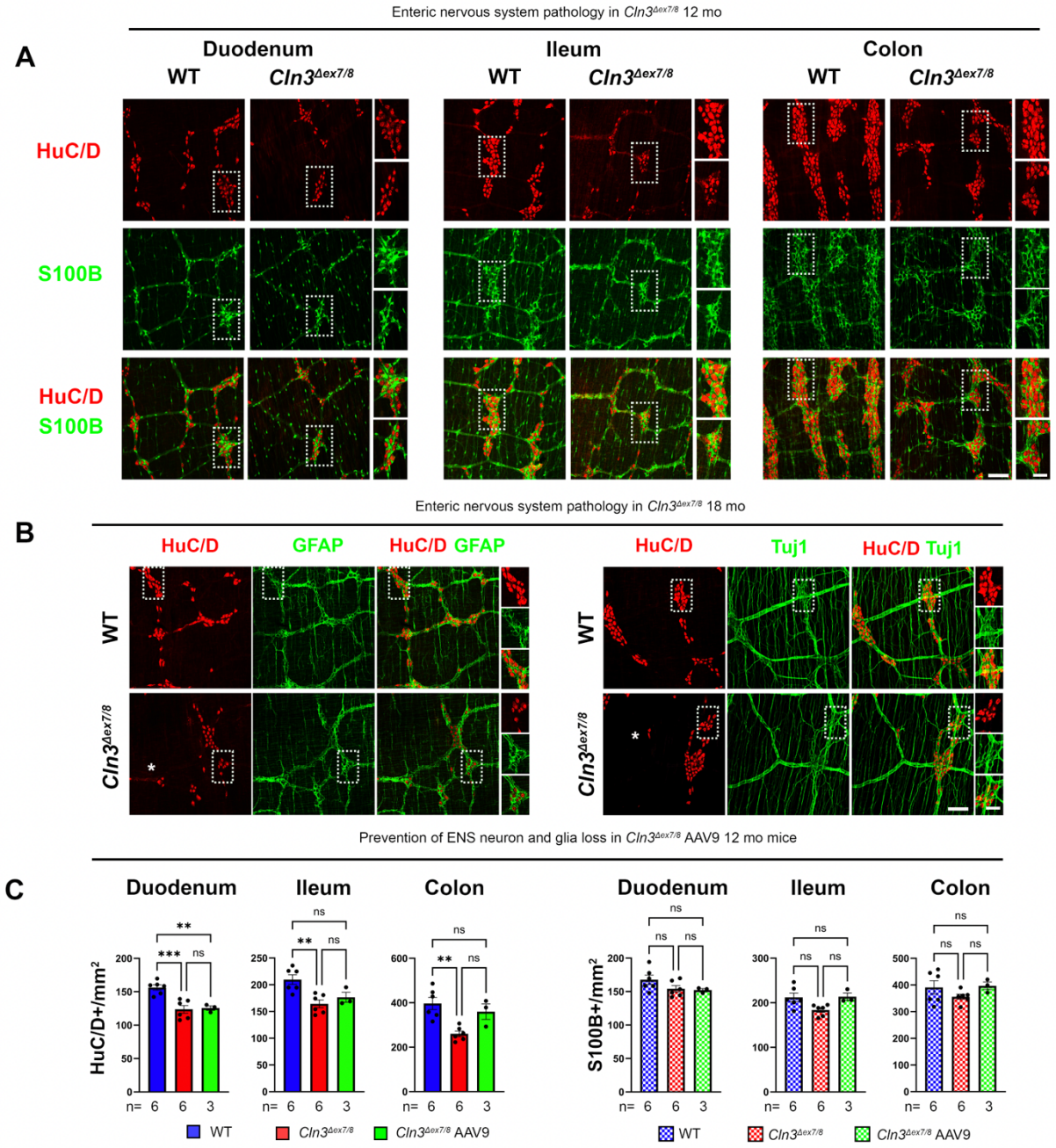

Fig. S2. Evidence for enteric nervous system pathology in *Cln3*$^{\Delta ex7/8}$ mice at 12 and 18 months. (A) Photomicrographs show immunostaining for HuC/D (neurons, red) and the glial marker S100B (green) in the duodenum, ileum and colon *Cln3*$^{\Delta ex7/8}$ mice and age-matched

wildtype (WT) controls at 12 months of age (mo). Scale bar 200μm, 50μm in higher power views. **(B)** Photomicrographs showing immunostaining for HuC/D (neurons, red) and either the glial marker glial fibrillary acidic protein (GFAP, green) or the neurofilament marker Tuj1 (green) in the duodenum *Cln3*$^{\Delta ex7/8}$ mice and age-matched WT controls at 18 months of age. Scale bar 200μm, 50μm in higher power views. Asterix (*) indicates regions of near complete enteric neuron loss. **(C)** Measurements of the density of HuC/D+ myenteric neurons and S100B+ myenteric glia reveal no significant differences (ns) in all bowel regions of 12-month-old *Cln3*$^{\Delta ex7/8}$ mice treated with AAV9-hCLN3 vs. untreated *Cln3*$^{\Delta ex7/8}$ mice. Data ± SEM. One-way ANOVA with a post-hoc Bonferroni correction, ** $p \leq 0.01$, *** $p \leq 0.001$.

***Cln3*$^{\Delta ex7/8}$ Histology Data 12 mo**

HuC/D	WT neurons/mm^2	*Cln3*$^{\Delta ex7/8}$ neurons/mm^2	Percent (%) Loss	p-value (WT vs. *Cln3*$^{\Delta ex7/8}$)
Duodenum	156.41±4.05	123.71±5.74	20.91%	p=0.0009
Ileum	209.63±9.00	164.22±7.28	21.66%	p=0.0029
Colon	396.73±27.24	260.12±12.61	34.43%	p=0.0011

S100B	WT S100B+ Ganglionic glia/ mm^2	*Cln3*$^{\Delta ex7/8}$ S100B+ Ganglionic glia/ mm^2	Percent (%) Loss	p-value (WT vs. *Cln3*$^{\Delta ex7/8}$)
Duodenum	167.73±6.78	154.08±4.76	8.14%	0.1305
Ileum	212.03±9.53	183.67±5.13	13.38%	0.0255
Colon	391.01±24.92	355.82±9.78	9.00%	0.2180

***Cln3*$^{\Delta ex7/8}$ Histology Data 18 mo**

HuC/D	WT neurons/mm^2	*Cln3*$^{\Delta ex7/8}$ neurons/mm^2	Percent (%) Loss	p-value (WT vs. *Cln3*$^{\Delta ex7/8}$)
Duodenum	182.60±5.31	106.15±4.69	41.87%	p<0.0001
Ileum	237.04±7.41	139.68±3.33	41.07%	p<0.0001
Colon	327.46±23.32	170.81±6.07	47.84%	p<0.0001

S100B	WT S100B+ Ganglionic glia/ mm^2	*Cln3*$^{\Delta ex7/8}$ S100B+ Ganglionic glia/ mm^2	Percent (%) Loss	p-value (WT vs. *Cln3*$^{\Delta ex7/8}$)
Duodenum	177.75±5.28	138.66±5.25	21.99%	0.0004
Ileum	239.25±5.26	186.71±2.24	21.96%	<0.0001
Colon	321.18±21.39	203.87±10.02	36.53%	0.0006

***Cln3$^{\Delta ex7/8}$* AAV9 Treated Histology Data 12 mo**

HuC/D	*Cln3$^{\Delta ex7/8}$* AAV9 neurons/mm^2	Percent (%) Loss *Cln3$^{\Delta ex7/8}$* AAV9 vs. WT	p-value (vs. WT)	Percent (%) Loss Untreated *Cln3$^{\Delta ex7/8}$* vs. WT	% Change Treated vs. Untreated *Cln3$^{\Delta ex7/8}$*
Duodenum	125.60±3.30	19.70%	0.0071	20.91%	101.53%
Ileum	176.65±9.36	15.73%	0.1014	21.66%	107.57%
Colon	359.92±34.64	9.28%	>0.9999	34.43%	138.37%

S100B	*Cln3$^{\Delta ex7/8}$* AAV9 Ganglionic glia/ mm^2	Percent (%) Loss *Cln3$^{\Delta ex7/8}$* AAV9 vs. WT	p-value (vs. WT)	Percent (%) Loss Untreated *Cln3$^{\Delta ex7/8}$* vs. WT	% Change Treated vs. Untreated *Cln3$^{\Delta ex7/8}$*
Duodenum	152.19±2.27	9.27%	0.2954	8.14%	98.77%
Ileum	213.65±8.34	-0.76%	>0.9999	13.38%	116.32%
Colon	397.00±14.38	-1.53%	>0.9999	9.00%	111.57%

***Cln3$^{\Delta ex7/8}$* AAV9 Treated Histology Data 18 mo**

HuC/D	*Cln3$^{\Delta ex7/8}$* AAV9 neurons/mm^2	Percent (%) Loss *Cln3$^{\Delta ex7/8}$* AAV9 vs. WT	p-value (vs. WT)	Percent (%) Loss Untreated *Cln3$^{\Delta ex7/8}$* vs. WT	% Change Treated vs. Untreated *Cln3$^{\Delta ex7/8}$*
Duodenum	141.86±6.31	22.31%	0.0003	41.87%	133.64%
Ileum	190.53±7.64	19.62%	0.0004	41.07%	136.40%
Colon	238.85±11.57	27.06%	0.0015	47.84%	139.83%

S100B	*Cln3$^{\Delta ex7/8}$* AAV9 Ganglionic glia/ mm^2	Percent (%) Loss *Cln3$^{\Delta ex7/8}$* AAV9 vs. WT	p-value (vs. WT)	Percent (%) Loss Untreated *Cln3$^{\Delta ex7/8}$* vs. WT	% Change Treated vs. Untreated *Cln3$^{\Delta ex7/8}$*
Duodenum	155.56±7.86	17.44%	0.0906	21.99%	105.83%
Ileum	222.49±5.88	12.45%	0.0894	21.96%	112.19%
Colon	267.51±6.87	18.97%	0.0273	36.53%	127.67%